doi: 10.1093/pasj/xxx000

Weak lensing clusters from HSC survey first-year data: Mitigating the dilution effect of foreground and cluster member galaxies

Takashi HAMANA[1,2], Masato SHIRASAKI[1] and Yen-Ting LIN[3]

[1]National Astronomical Observatory of Japan, Mitaka, Tokyo 181-8588, Japan
[2]The Graduate University for Advanced Studies, SOKENDAI, Mitaka, Tokyo 181-8588, Japan
[3]Academia Sinica Institute of Astronomy and Astrophysics, P.O. Box 23–141, Taipei 10617, Taiwan

Received 2020 July 1; Accepted 2020 July 1

Abstract

We present a weak lensing cluster search using Hyper Suprime-Cam Subaru Strategic Program (HSC survey) first-year data. We pay special attention to the dilution effect of cluster member and foreground galaxies on weak lensing signals from clusters of galaxies; we adopt the globally normalized weak lensing estimator which is least affected by cluster member galaxies, and we select source galaxies by using photometric redshift information to mitigate the effect of foreground galaxies. We produce six samples of source galaxies with different low-z galaxy cuts, construct weak lensing mass maps for each of the source sample, and search for high peaks in the mass maps that cover an effective survey area of $\sim$120 deg^2. We combine six catalogs of high peaks into a sample of cluster candidates which contains 124 high peaks with signal-to-noise ratios greater than five. We cross-match the peak sample with the public optical cluster catalog constructed from the same HSC survey data to identify cluster counterparts of the peaks. We find that 107 out of 124 peaks have matched clusters within 5 arcmin from peak positions. Among them, we define a sub-sample of 64 secure clusters that we use to examine dilution effects on our weak lensing cluster search. We find that source samples with the low-z galaxy cuts mitigate the dilution effect on weak lensing signals of high-z clusters ($z \gtrsim 0.3$), and thus combining multiple peak catalogs from different source samples improves the efficiency of weak lensing cluster searches.

Key words: galaxies: clusters: general — cosmology: observations — dark matter — large-scale structure of universe

1 Introduction

Clusters of galaxies have been playing important roles in the modern cosmology: Their abundance and evolution have been used to place constraints on cosmological parameters (Allen et al. 2011), and their baryonic components (galaxies and hot intra-cluster gas) have been used to study physical processes of hierarchical structure formation in the universe (Kravtsov & Borgani 2012). In those studies, a large sample of clusters of galaxies is the fundamental data, which has been constructed by identifying their tracers such as optical galaxy concentrations, X-ray emissions, Sunyaev-Zel'dovich effect (SZE), and dark matter concentrations via the weak lensing technique (Pratt et al. 2019). Since all cluster mass-observable relations have scatters, sample completeness in terms of the cluster mass, which is the principal quantity to link an observation to a theory, varies from method to method. Weak lensing cluster finding is unique in that it uses the matter concentration as the tracer regardless of physical state of baryonic components, enabling one to locate under-luminous (in optical/X-ray/SZE) clusters.

Observationally, there are two conflicting difficulties in constructing a sizable cluster sample with weak lensing in a practical time scale; a wide survey area to locate rare objects, and a deep imaging to achieve a sufficient number density of source galaxies. Thanks to the development of wide-field optical cameras with dedicated wide field surveys, weak lensing cluster finding has made rapid progress in the last two decades, (see Table 1 of Miyazaki et al. 2018a, and references therein). Recently, Miyazaki et al. (2018a) have conducted a weak lensing cluster search in a $\sim$160 deg^2 area of Hyper Suprime-Cam Subaru Strategic Program (hereafter, HSC survey, Aihara et al. 2018b) first-year data (Aihara et al. 2018a; Mandelbaum et al. 2018a), and have reported a detection of 65 peaks[1] with signal-to-noise ratio (SN) greater than 4.7 in weak lensing mass maps. They have cross-matched the peaks with optical cluster catalogs and found that 63 out of 65 peaks had optical counterparts, demonstrating that a wide field survey with a sufficient depth (for their case $i = 24.5$ mag) is indeed able to yield a sizable and high purity cluster sample.

In the near future, the size of weak lensing cluster sample will become much larger as many more wide-area weak lensing-oriented surveys will come: The final survey area of HSC survey is 1400 deg^2 (more than eight times of the first-year data), and Legacy Survey of Space and Time (LSST, Ivezić et al. 2019) and Euclid survey (Laureijs et al. 2012; Racca et al. 2018) will cover a large portion of the sky with a sufficient depth. It is thus worth improving methods of weak lensing cluster finding by making best use of multi-band dataset that on-going/future surveys take. This is exactly the purpose of this paper.

In this paper, we focus on the dilution effect that we briefly explain below: Weak lensing effect by clusters distorts shapes of background galaxies in a coherent manner. Since the shape distortions by weak lensing (lensing shear), which are generally smaller than intrinsic ellipticities of galaxies, can not be extracted from individual galaxies, a lensing analysis necessarily involves averaging of shear estimators among a sample of galaxies to derive lensing shears and to suppress the noise from intrinsic ellipticities (called the shape noise). If a galaxy sample used for a weak lensing analysis contains not only background lensed galaxies but also foreground and/or cluster member galaxies which are not affected by cluster lensing and thus have no lensing signal, the latter acts as contaminants in weak lensing analyses and *dilutes* the lensing signals by clusters (see Broadhurst et al. 2005; Limousin et al. 2007; Hoekstra 2007; Medezinski et al. 2007; Umetsu & Broadhurst 2008; Okabe et al. 2010, for observational studies of the dilution effects in analyses of cluster lensing). In most of recent lensing analyses of individual clusters with known redshifts, source galaxies are selected using multi-band galaxy photometry data so that the contamination of foreground and cluster member galaxies is minimized (see Medezinski et al. 2018, and references therein). However, in weak lensing cluster findings, redshifts of clusters are unknown in advance, and thus a galaxy sample was commonly selected by a simple magnitude-cut on a single band photometry (for example, Miyazaki et al. 2002; Hamana et al. 2015). Such a galaxy sample inevitably contains foreground/cluster member galaxies and suffers from the dilution effect.

Weak lensing cluster finding is based on peak heights in mass maps. The detection threshold is set by the peak height SN considering the trade-off between completeness and purity (lowering the threshold SN leads to a larger number of cluster detections at the cost of a higher false detection rate). However, the peak heights of cluster lensing are indeed affected by the dilution effect. Its direct impact is the decline in numbers of cluster detections. Another impact is on theoretical models of weak lensing mass map peaks; incorporating its effect into theoretical models requires a realistic modeling of the dilution effect which is most likely dependent on cluster mass, redshift, and galaxy selection criteria (for example, the detection band, magnitude-cut, and size-cut). Therefore it is fundamentally important to understand actual dilution effects on weak lensing mass maps on a case-by-case basis.

The purpose of this paper is two-fold: The first is to develop a weak lensing cluster finding method that mitigates the dilution effects by incorporating photometric redshift information of galaxies. We apply it to the HSC survey first-year data in which both the weak lensing shape catalog and photometric redshift data are publicly available (Mandelbaum et al. 2018a; Tanaka et al. 2018). We present a sample of weak lensing peaks located by our finding method. We identify their counterpart clusters by cross-matching with the optical cluster catalog (Oguri et al. 2018). Using the derived weak lensing cluster sample, we examine the dilution effects on actual weak lensing mass maps in an empirical manner, which is our second

[1] In this paper, we use the term "peak" to mean a local maximum on a weak lensing mass map with its height exceeding a given threshold (see Section 3.3 for details). We adopt the signal-to-noise ratio (SN) of mass maps (see Section 3.2 for its definition) to define the threshold, because the noise in the mass map originating from intrinsic galaxy shapes is well characterized by the random Gaussian field (van Waerbeke 2000), and thus it gives a rough estimate of a significance of a peak.

purpose.

The structure of this paper is as follows. In Section 2, we briefly summarize the HSC survey first-year shear catalog and the photometric redshift data used in this study. In Section 3, we describe the methods to generate a sample of weak lensing peaks, including the selection of source galaxies, the method to reconstruct weak lensing mass maps, and the peak finding algorithm. In Section 4, we cross-match the weak lensing peaks with a sample of optical clusters to identify their cluster counterparts. Then we examine fundamental properties of weak lensing clusters detected by our method. In Section 5, we examine the dilution effects of foreground and cluster member galaxies on our weak lensing peaks in an empirical manner using actual source galaxy samples and empirical models. Finally, we summarize and discuss our results in Section 6. In Appendix 1, we present results of cross-matching of our sample of weak lensing peaks with selected catalogs of known clusters. In Appendix 2, we describe systems of neighboring peaks in our peak sample. In Appendix 3, we present results of the cluster mass estimate of the weak lensing peak sample based on a model fitting to weak lensing shear profiles. In Appendix 4, we compare the globally normalized SN estimator, which is adopted in this study, with the locally normalized SN estimator adopted in some previous studies (for example, Hamana et al. 2015).

Throughout this paper, unless otherwise stated, we adopt the cosmological model with the cold dark matter (CDM) density $\Omega_{\rm cdm}=0.233$, the baryon density $\Omega_{\rm b}=0.046$, the matter density $\Omega_{\rm m}=\Omega_{\rm cdm}+\Omega_{\rm b}=0.279$, the cosmological constant $\Omega_\Lambda=0.721$, the spectral index $n_s=0.97$, the normalization of the matter fluctuation $\sigma_8=0.82$, and the Hubble parameter $h=0.7$, which are the best-fit cosmological parameters in the Wilkinson Microwave Anisotropy Probe (WMAP) 9-year results (Hinshaw et al. 2013).

2 HSC survey data

In this section, we briefly describe those aspects of the HSC survey first year products that are directly relevant to this study, see the following references for full details: Aihara et al. (2018b) for an overview of the HSC survey and survey design, Aihara et al. (2018a) for the first public data release, Miyazaki et al. (2018b); Komiyama et al. (2018); Kawanomoto et al. (2018); Furusawa et al. (2018) for the performance of the HSC instrument itself, Bosch et al. (2018) for the optical imaging data processing pipeline used for the first-year data, Mandelbaum et al. (2018a) for the first-year shape catalog, Mandelbaum et al. (2018b) for the calibration of galaxy shape measurements with image simulations, Aihara et al. (2019) for the public data release of the first-year shape catalog, and Tanaka et al. (2018) for photometric redshifts derived for the first-year data.

2.1 HSC first-year shape catalog

We use the HSC first-year shape catalog (Mandelbaum et al. 2018a), in which the shapes of galaxies are estimated on the i-band coadded image adopting the re-Gaussianization PSF correction method (Hirata & Seljak 2003). Only galaxies that pass given selection criteria are included in the catalog. Among others, the four major criteria, which are relevant to the following analyses, for galaxies to be selected are,

(1) *full-color and full-depth cut*: the object should be located in regions reaching approximately full survey depth in all five ($grizy$) broad bands,
(2) *magnitude cut*: the i-band cmodel magnitude (corrected for extinction) should be brighter than 24.5 AB mag,
(3) *resolution cut*: the galaxy size normalized by the PSF size, which varies from position to position on coadded images depending on observational condition, defined by the re-Gaussianization method, should be larger than a given threshold of `ishape_hsm_regauss_resolution` $\geq$ `0.3`,
(4) *bright object mask cut*: the object should not be located within the bright object masks.

See Table 4 of Mandelbaum et al. (2018a) for the full description of the selection criteria.

The HSC shape catalog contains all the basic parameters needed to perform weak lensing analyses in this study. The following five sets of parameters for each galaxy are directly relevant to this study (see Mandelbaum et al. 2018a, for a detail description of each item); (1) the two-component distortion, $\boldsymbol{e}=(e_1,e_2)$, which represents the shape of each galaxy image, (2) shape weight, w, (3) intrinsic shape dispersion per component, $e_{\rm rms}$, (4) multiplicative bias, m, and (5) additive bias, (c_1,c_2).

2.2 Photometric redshifts

Using the HSC five-band photometry, photometric redshift (hereafter photo-z) was estimated with six independent codes, described in detail in Tanaka et al. (2018). In this study, we adopt `Ephor AB` photo-z data which were derived from the PSF-matched aperture photometry (called the `afterburner` photometry) using a neural network code, `Ephor`[2]. The data-set contains not only the point estimate

[2] https://hsc-release.mtk.nao.ac.jp/doc/index.php/photometric-redshifts/.

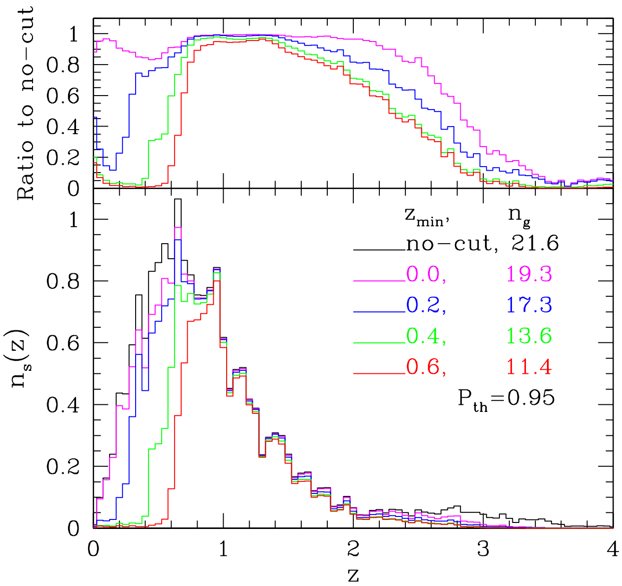

Fig. 1. *Bottom panel*: Estimates of redshift distribution of the source samples computed by summing up the redshift probability distribution, $P(z)$, over selected source galaxies [see equation (2)]. The normalization is taken so that $\int dz n_s(z) = 1$ for the "no-cut" case (i.e. the full galaxy sample) shown in black histogram. *Top panel*: Ratio of the redshift distribution for a source sample to that of "no-cut" case.

but also the probability distribution function of the redshift for each galaxy, that we use to select source galaxies (see Section 3.1).

3 Weak lensing mass maps and high SN peaks

In this section, we describe our procedure for constructing a sample of high SN peaks located in weak lensing mass maps.

3.1 Source galaxy selection

We use the photo-z information to select source galaxies which are used in constructing weak lensing mass maps (detailed in the next subsection). We adopt the *P-cut* method proposed by Oguri (2014) that uses the full probability distribution function of redshift, denoted by $P(z)$, for each galaxy estimated by the `ephor` method; we define samples of source galaxies that satisfy

$$P_{int} \equiv \int_{z_{\rm min}}^{z_{\rm max}} P(z)\ dz > P_{th}, \tag{1}$$

with the threshold integrated probability of $P_{th} = 0.95$. Our main aim here is to mitigate the dilution effects of foreground and cluster member galaxies, and thus a choice of $z_{\rm max}$ is not crucial as long as it does not so much reduce the number density of source galaxies. In this study, we take $z_{\rm max} = 3$. Since we do not know redshifts of clusters to be located in mass maps in advance, we take multiple choices of $z_{\rm min}$; to be specific, we take $z_{\rm min} = 0$, 0.2, 0.3, 0.4, 0.5, and 0.6.

The summation of $P(z)$ over selected galaxies gives a reasonably reliable estimate of redshift distribution of the source sample[3]. Taking the lensing weight (w_i) into account, we have

$$n_s(z) = \sum_i w_i P_i(z). \tag{2}$$

The effective redshift distributions derived by this method are shown in Fig. 1 in comparison with the full galaxy sample. It is seen in the Figure that the *P-cut* method works well to suppress the probability that source samples include galaxies being at outside the given redshift ranges. The mean source galaxy number densities for each sample are summarized in Table 1.

3.2 Weak lensing mass reconstruction

The weak lensing mass map which is the smoothed lensing convergence field (κ) is evaluated from the tangential shear data by (Schneider 1996)

$$\mathcal{K}(\boldsymbol{\theta}) = \int d^2\boldsymbol{\phi}\ \gamma_t(\boldsymbol{\phi}:\boldsymbol{\theta}) Q(|\boldsymbol{\phi}|), \tag{3}$$

where $\gamma_t(\boldsymbol{\phi}:\boldsymbol{\theta})$ is the tangential component of the shear at position $\boldsymbol{\phi}$ relative to the point $\boldsymbol{\theta}$, and Q is the filter function for which we adopt the truncated Gaussian function (for κ field) (Hamana et al. 2012),

$$Q(\theta) = \frac{1}{\pi\theta^2}\left[1 - \left(1 + \frac{\theta^2}{\theta_G^2}\right)\exp\left(-\frac{\theta^2}{\theta_G^2}\right)\right], \tag{4}$$

for $\theta < \theta_o$ and $Q = 0$ elsewhere. The filter parameters should be chosen so that signals (high peaks in weak lensing mass maps) from expected target clusters (i.e. $M_{\rm vir} > 10^{14} h^{-1} M_\odot$ at $0.1 < z < 0.6$) become largest (see Hamana et al. 2004). We take $\theta_G = 1.5$ arcmin and $\theta_o = 15$ arcmin.

In our actual computation, $\mathcal{K}$ is evaluated on regular grid points with a grid spacing of 0.15 arcmin. Since galaxy positions are given in the sky coordinates, we use the tangent plane projection to define the grid. On and around regions where no source galaxy is available due to imaging data being affected by bright stars or large nearby galaxies, $\mathcal{K}$ may not be accurately evaluated. We define "data-region", "masked-region" and "edge-region" by using the distribution of source galaxies as follows: First, for each grid point, we check if there is a galaxy within 0.75 arcmin (about three times the mean galaxy separation) from

[3] Notice that the stacking photo-z $P(z)$ is not a mathematically sound way to infer the true redshift distribution (see Section 5.2 of Hikage et al. 2019).

Table 1. Summary of source galaxy samples: Total area of data-region (see Section 3.2 for its definition), The effective number density of source galaxies defined by equation (1) of Heymans et al. (2012) ($\bar{n}_g$), the averaged shape noise ($\langle\sigma^2_{\rm shape}\rangle^{1/2}$), and numbers of peaks with $SN \geq 5$. The last column lists the numbers of merged peaks with $z_{\rm opt} = z_{\rm min}$ (i.e., a peak's $SN_{\rm max}$ comes from that source sample) with numbers in the parentheses being those not existing in $z_{\rm min} = 0$ sample with $SN(z_{\rm min} = 0) \geq 5$.

$z_{\rm min}$	Area [deg^{-2}]	$\bar{n}_g$ [arcmin^{-2}]	$\langle\sigma^2_{\rm shape}\rangle^{1/2}$	$N_{\rm peak}$ $SN \geq 5$	$N_{\rm peak}$[merged] at $z_{\rm opt}$ $SN_{\rm max} > 5$
0.0	120.01	19.3	0.0158	68	24 (-)
0.2	119.51	17.2	0.0167	71	14 (3)
0.3	118.90	15.2	0.0179	70	18 (9)
0.4	118.08	13.6	0.0190	75	22 (13)
0.5	117.50	12.7	0.0198	73	15 (8)
0.6	116.63	11.4	0.0209	69	31 (23)

Table 2. The effective survey area of each field. This is for the source sample with $z_{\rm min} = 0$. Total areas of other source sample are summarized in Table 1.

Field name	Data-region area^a [deg^2]
XMM	26.30
GAMA09H	28.52
WIDE12H	11.45
GAMA15H	27.50
HECTOMAP	9.48
VVDS	16.77
total	120.01

[a] Area after removing regions affected by bright objects (masked-region) and edge-region in unit of degree^2. See Section 3.2 for the definitions of those regions.

the grid point. If there is no galaxy, then the grid point is flagged as "no-galaxy". After performing the procedure for all the grid points, all the "no-galaxy" grid points plus all the grid points within 0.75 arcmin from all the "no-galaxy" grid points are defined as the "masked-region". All the masked-regions are excluded from our weak lensing analysis. All the grid points located within 1.5 arcmin (we take this value by setting it equal to θ_G) from any of masked-region grid points are defined as the "edge-region". All the rest of grid points are defined as the "data-region". Since the sky distribution of galaxies differs among different source samples, we carry out this procedure for every source sample. The total survey areas (data-region) of each source sample are summarized in Table 1, and areas of six fields for $z_{\rm min} = 0$ sample are summarized in Table 2. The difference in the total areas among different source samples is not large but 3 percent at largest. The total areas of the edge-region are ~ 30 degree^2, accounting for ~ 20 percent of the data- plus edge-region.

On grid points, $\mathcal{K}$ is evaluated using equation (3), but the integral in that equation is replaced with a summation over galaxies;

$$\mathcal{K}(\boldsymbol{\theta}) = \frac{1}{\bar{n}_g}\sum_i \hat{\gamma}_{t,i} Q(|\boldsymbol{\phi_i}|), \tag{5}$$

where the summation is taken over galaxies within θ_o from a grid point at $\boldsymbol{\theta}$, $\hat{\gamma}_{t,i}$ is an estimate of tangential shear of i-th galaxy at the angular position $\boldsymbol{\phi_i}$ from the grid point, and $\bar{n}_g$ is the mean galaxy number density (see Section 5.1 and Appendix 4 for discussion on our choice of the *global normalization*, and see also Schmidt & Rozo 2011 for a related study). The noise on mass maps coming from intrinsic shapes of galaxies is evaluated on each grid point (Schneider 1996),

$$\sigma^2_{\rm shape}(\boldsymbol{\theta}) = \frac{1}{2\bar{n}_g^2}\sum_i \hat{\gamma}_i^2 Q^2(|\boldsymbol{\phi_i}|). \tag{6}$$

We define the signal-to-noise ratio (SN) of weak lensing mass map by

$$SN(\boldsymbol{\theta}) = \frac{\mathcal{K}(\boldsymbol{\theta})}{\langle\sigma^2_{\rm shape}\rangle^{1/2}}, \tag{7}$$

where $\langle\sigma^2_{\rm shape}\rangle$ is the mean value over all the grids in the data-region.

Taking the lensing weight, which we normalized so that the total weight equals the total number of galaxies (i.e., $\sum_i w_i = N_g$), and measurement biases into account, equation (5) is modified to (Mandelbaum et al. 2018a),

$$\mathcal{K}(\boldsymbol{\theta}) = \frac{1}{\bar{n}_g}\frac{\sum_i w_i(e_{t,i}/2\mathcal{R} - \hat{c}_t)Q(|\boldsymbol{\phi_i}|)}{1+\hat{m}}, \tag{8}$$

where e_t is the tangential component of distortion taken from the HSC shape catalog. Sample averaged multiplicative bias, responsibity factor and additive bias are given as follows,

$$\hat{m} = \frac{\sum_i w_i m_i}{\sum_i w_i}, \tag{9}$$

$$\mathcal{R} = 1 - \frac{\sum_i w_i e^2_{{\rm rms},i}}{\sum_i w_i}, \tag{10}$$

and

$$\hat{c}_t = \frac{\sum_i w_i c_{t,i}}{\sum_i w_i}, \qquad (11)$$

where $c_{t,i}$ is the tangential component the additive bias for each galaxy. Similarly, the expression for the shape noise, equation (6), is modified to,

$$\sigma^2_{\rm shape}(\boldsymbol{\theta}) = \frac{1}{2\bar{n}_g^2} \frac{\sum_i w_i^2 (e_{t,i}/2\mathcal{R} - \hat{c}_t)^2 Q^2(|\boldsymbol{\phi_i}|)}{(1+\hat{m})^2}. \qquad (12)$$

3.3 Peak finding and merging multiple peak catalogs

We first apply the weak lensing mass reconstruction to each sample of source galaxies. We define a peak in the generated mass maps as the grid point with SN value being higher than all the surrounding eight grid points. We first select peaks with $SN \geq 4$ located in the data-region. If there is a pair of peaks with separation smaller than $\sqrt{2} \times \theta_G \simeq 2.1$ arcmin, the lower SN peak of the pair is discarded to avoid multiple peaks from a single cluster (due to, for example, substructures of clusters).

The numbers of peaks with $SN \geq 5$ for six source samples are summarized in Table 1. Note that only peaks located in the data-region are included in the peak catalogs. In the same Table, the mean shape noise values measured from each sample are summarized, which scale with the galaxy number density approximately as $\langle \sigma^2_{\rm shape} \rangle \propto \bar{n}_g^{-1}$ as expected (Schneider 1996). It should be noticed that although the shape noise becomes larger for higher $z_{\rm min}$ samples, the number of peak detection does not always decrease. This may indicate that our source sample selection with a low-z cut indeed mitigates the dilution effects, that we will go into detail in Section 5.

We combine the six catalogs of high peaks ($SN \geq 4$) from different source samples by matching peak positions to a tolerance of $2 \times \theta_G = 3$ arcmin. Most of peaks have multiple matches. Matched peaks from different source samples are merged and are considered as peaks from the same cluster, and the highest SN among matched peaks is taken as its peak SN that we denote $SN_{\rm max}$ and we define its source sample's $z_{\rm min}$ as $z_{\rm opt}$. There are 124 merged peaks with $SN_{\rm max} \geq 5$, which we take as our primary sample of cluster candidates. In Table 3, basic information of those 124 merged peaks are summarized.

In the last column of Table 1, we present numbers of merged peaks for each $z_{\rm opt} = z_{\rm min}$ with numbers in the parentheses showing those that do not exist in the $z_{\rm min} = 0$ sample. We see that $z_{\rm opt}$ is distributed rather broadly with a noticeable number at the highest $z_{\rm min}$ sample. It is found that 56 out of 124 merged peaks have $SN(z_{\rm min} = 0) < 5$ (to be specific, SNs of those peaks measured in mass maps from $z_{\rm min} = 0$ source sample are smaller than 5). This may be an indication that the dilution effects indeed have non-negligible influence on peak SNs in mass maps of $z_{\rm min} = 0$.

4 Cross-matching with CAMIRA-HSC clusters

We cross-match our merged peak catalog with the CAMIRA (Cluster-finding Algorithm based on Multi-band Identification of Red-sequence gAlaxies, Oguri 2014) HSC cluster sample to identify clusters of galaxies from which weak lensing peak signals originate. CAMIRA-HSC cluster sample is based on the same HSC S16A data set (Oguri et al. 2018) used in our study, and thus covers our survey fields uniformly except for regions affected by blight objects. We take this optically-selected cluster catalog as our primary reference sample, because it covers a sufficiently wide redshift range ($0.1 < z < 1.1$) and cluster mass range (the richness $N_{mem} > 15$, where richness is defined as the effective number of member galaxies above stellar mass greater than $10^{10.2} M_\odot$). For each cluster, the sky coordinates and cluster redshifts based on the red sequence of cluster member galaxies are estimated (see details of cluster finding algorithm and definitions of those quantities, Oguri 2014; Oguri et al. 2018), that we use in the following analysis. See Appendix 1 for results of cross-matching with other selected cluster samples.

We cross-match our merged peak catalog with CAMIRA-HSC clusters[4] with their positions to a tolerance of 5 arcmin. We summarize the results in Table 1, in which the angular separation between a peak position and a matched CAMIRA-HSC cluster position is given ($\theta_{\rm sep}$). Since the smoothing scale of weak lensing mass map is $\theta_G = 1.5$ arcmin, the tolerance radius could be large enough to identify clusters of galaxies from which the weak lensing peaks originate. However, 17 out of 124 peaks have no CAMIRA-HSC cluster counterpart (see Appendix 1.1 for some details of those peaks). Among the rest of 107 peaks, 25 peaks have multiple matches (mostly matching with two CAMIRA-HSC clusters, but 3 out of 25 peaks have three matches). There are some possible reasons for those systems: Some of such peaks could be due to physically interacting nearby cluster systems, but others could be generated not from a single system but from a line-of-sight projection of multiple clusters (Hamana et al. 2004). In this paper, we are not going into details of such multiple-match peaks.

Among 82 peaks matching with a single CAMIRA-HSC

[4] There are some different CAMIRA-HSC catalogs based on different HSC data sets. We use the HSC wide cluster catalog based on HSC S16A data with updated star mask called 'Arcturus' (Mandelbaum et al. 2018a). The catalog is available from https://www.slac.stanford.edu/˜oguri/cluster/.

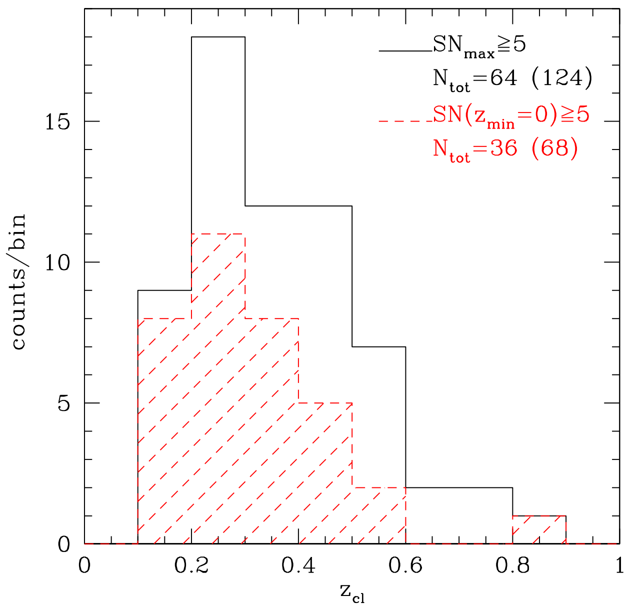

Fig. 2. Black histogram shows the redshift distribution of the weak lensing secure clusters (64 out of 124 merged peaks), whereas the red hatched histogram shows the same clusters but having $SN \geq 5$ in weak lensing mass maps from the source sample of $z_{\rm min} = 0$ (36 out of 68 peaks located in $z_{\rm min} = 0$ mass maps with $SN \geq 5$).

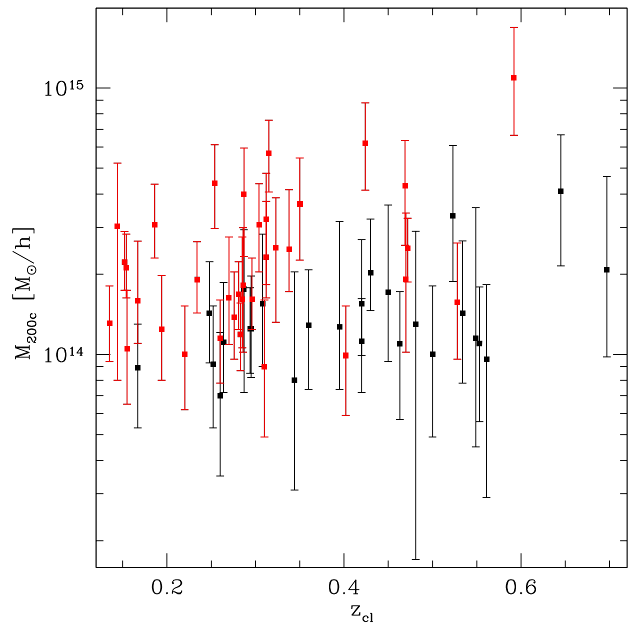

Fig. 3. Distribution of weak lensing secure clusters on the $M_{200c} - z_{cl}$ plane. The cluster masses defined by the spherical over-density mass M_{200c} are derived by fitting the NFW model to measured weak lensing shear profiles based on the standard likelihood analysis (see Appendix 3), and filled squares and error bars show the peak and 68.3% confidence interval of the posterior distributions. Red (black) symbols are for clusters with the peak $SN \geq 5$ (< 5) in weak lensing mass maps from the source sample of $z_{\rm min} = 0$.

cluster, 64 peaks have CAMIRA-HSC cluster counterparts within 2 arcmin from peak positions. Although it is possible that some of those peaks are affected by line-of-sight projections of small clusters (below the richness threshold of CAMIRA algorithm), it is highly likely that the major lensing contribution comes from the matched CAMIRA-HSC clusters. We have also visually inspected those systems with HSC *riz*-color image, and found good correlations between weak lensing mass over-densities and galaxy concentrations for all the cases. We thus define those 64 peaks as the *secured sample of WL clusters*, with redshift (that we denote z_{cl}) taken from the matched CAMIRA-HSC cluster, which we will use to investigate the dilution effects in the following section. The redshift distribution of those secured weak lensing clusters is shown in Figure 2. In the same plot, we also show the distribution of those weak lensing secure clusters that have $SN \geq 5$ in weak lensing mass maps from the source sample of $z_{\rm min} = 0$. Comparing the two distributions, we see that a large part of clusters at $z_{cl} > 0.4$ have peak SNs below our threshold of $SN = 5$ in the mass maps of $z_{\rm min} = 0$, and pass the threshold in mass maps of $z_{\rm min} \geq 0.2$.

We derive the cluster masses of the weak lensing secure clusters by fitting the NFW model to measured weak lensing shear profiles based on the standard likelihood analysis (see Appendix 3 for details). Derived cluster masses are plotted on the cluster mass–redshift plane in Figure 3, where red (black) symbols are for clusters with the peak $SN \geq 5 (< 5)$ in weak lensing mass maps from the source sample of $z_{\rm min} = 0$. From this Figure, we find that clusters below the peak height threshold ($SN = 5$) in the mass maps of $z_{\rm min} = 0$ are mostly relatively lower mass clusters at $z_{cl} \gtrsim 0.4$. This is a natural result of the following two facts that (1) for a fixed cluster redshift, the peak height is higher for more massive clusters (Hamana et al. 2004), and (2) the dilution effect of foreground galaxies is stronger for higher redshift clusters and for lower $z_{\rm min}$ galaxy samples (see the next section).

5 Dilution effects on weak lensing peaks from clusters

The dilution effects on weak lensing high peaks originating from clusters are caused by foreground and cluster member galaxies (for observational studies of the dilution effects in analyses of cluster lensing, see for example Broadhurst et al. 2005; Okabe et al. 2010; Medezinski et al. 2018). Let us first make a rough estimate of proportions of those galaxies in our source galaxy samples. We see from the estimated redshift distributions of source samples shown in Figure 1 that a proportion of foreground to background

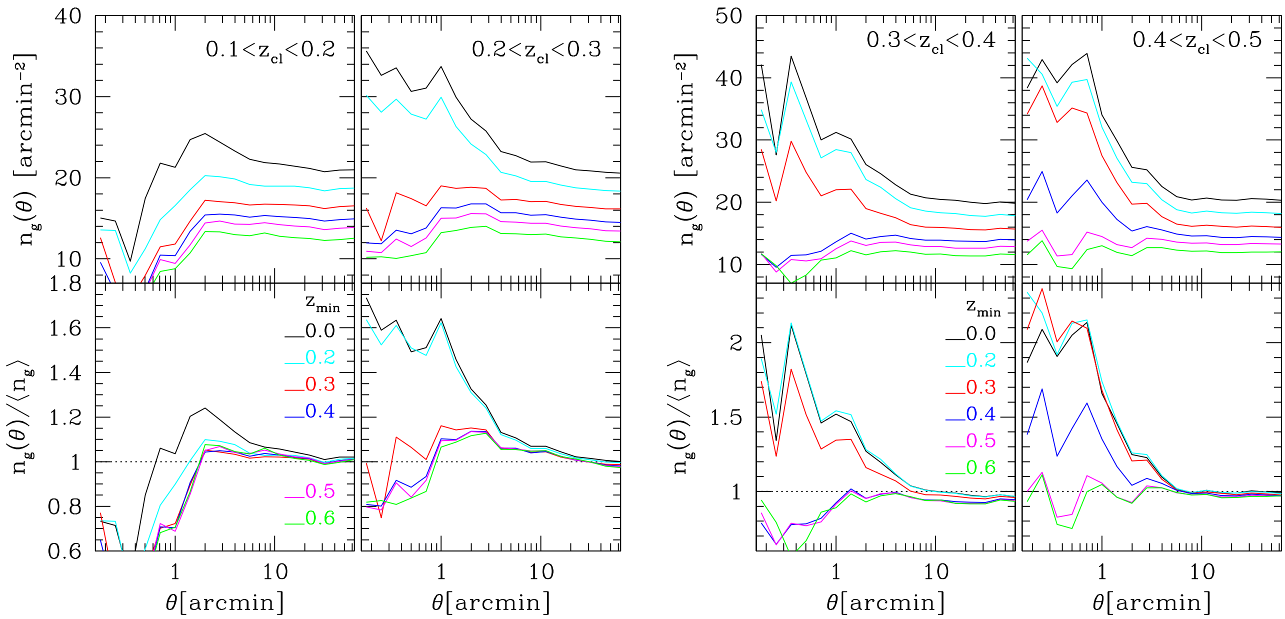

Fig. 4. *Top-panels*: Stacked galaxy number density profiles as a function of angular radius from peak positions. Samples of the weak lensing secure clusters (defined in Section 4) with cluster redshifts within a given redshift range (denoted in each panel) are used. Different colors are for different source galaxy samples characterized by $z_{\rm min}$ (see Section 3.1). *Bottom-panels*: The same stacked galaxy number density profiles shown in the top-panels but normalized by the mean number density of each source galaxy sample.

galaxies depends strongly on both cluster redshifts and source samples, and it can be more than 20 percent for high-z clusters in low-$z_{\rm min}$ source samples. We estimate the proportion of cluster member galaxies by measuring stacked galaxy number density profiles of sub-samples of weak lensing secure clusters selected based on cluster redshifts. The measurement is done for every source galaxy sample and the results are presented in Figure 4 for four redshift ranges. We find that, at cluster central regions, a considerable number of cluster member galaxies are contained in source samples with $z_{\rm min} < z_{cl}$ except for the case of the lowest cluster redshift range. The excess mostly disappears in source samples with $z_{\rm min} > z_{cl}$. However, we note that the degree of the excess and its suppression largely vary from cluster to cluster.

We have adopted two means to mitigate the dilution effects: One is to take the *globally normalized* SN estimator, equation (7) with equations (5) and (6), and the other is to combine multiple peak catalogs from weak lensing mass maps of source samples with different $z_{\rm min}$. In the following sub-sections, we will first describe the former, then we will examine the effectiveness of the latter using actual source galaxy samples.

Another important point seen in Figure 4 is that the deficiency of source galaxies in cluster central regions for the lowest redshift cluster sample and for the other samples with $z_{\rm min} > z_{cl}$. There are two possible causes of this: One is the masking effect of bright cluster galaxies that screen background galaxies behind them. The other is the lensing magnification effect that enlarges a sky area behind clusters resulting in a decrease in the local galaxy number density (for more details, see Bartelmann & Schneider 2001; and see Chiu et al. 2019 for a measurement of lensing magnification effect in the HSC data). We are not going into further details of those two effects because it is beyond the scope of this paper, but we examine their influence on the peak height using empirical models in Section 5.3.

5.1 The globally normalized SN estimator

Here, we explain how the globally normalized SN estimator defined by equation (7) can mitigate the dilution effect of cluster member galaxies. We examine actual advantage of this estimator over the locally normalized estimator in Appendix 4.

Let us assume the following simple model of a galaxy distribution which consists of three populations; lensed background galaxies (bg), unlensed foreground galaxies (fg), and unlensed cluster member galaxies (cl), with number densities of n_{bg}, n_{fg}, and $n_{cl}(\theta)$, respectively. Note that we have assumed that only $n_{cl}(\theta)$ has a non-uniform sky distribution associated with clusters of galaxies. As is seen in Figure 4, $n_{cl}(\theta)$ can be comparable to $n_{bg}+n_{fg}$ at cluster central regions. However, since the cluster population is very rare in the sky, in what follows, we assume that the globally averaged $n_{cl}(\theta)$ is much smaller than $n_{bg}+n_{fg}$, and we take $\bar{n}_g = n_{bg} + n_{fg}$. Then the globally normalized estimator, equation (5), can be formally written by

$$\mathcal{K}_G(\boldsymbol{\theta}) = \frac{1}{\bar{n}_g}\sum_i \hat{\gamma}_{t,i}Q_i = \frac{1}{\bar{n}_g}\left(\sum_{i\in bg}\hat{\gamma}_{t,i}Q_i + \sum_{i\in fg}\hat{\gamma}_{t,i}Q_i + \sum_{i\in cl}\hat{\gamma}_{t,i}Q_i\right) = \frac{1}{n_{fg}+n_{bg}}\sum_{i\in bg}\hat{\gamma}_{t,i}Q_i, \quad (13)$$

where from the second to third line, we have used the fact that the foreground and cluster member galaxies have no lensing signal. Denoting the galaxy intrinsic ellipticity by $e^{\rm int}$ and its shear converted one by $\hat{e} = e^{\rm int}/2\mathcal{R}$, the estimator of the shape noise, equation (6), can be written, in the same manner, by

$$\sigma^2_{{\rm shape},G}(\boldsymbol{\theta}) = \frac{1}{2(n_{fg}+n_{bg})^2} \times \left(\sum_{i\in bg}\hat{e}_i^2Q_i^2 + \sum_{i\in fg}\hat{e}_i^2Q_i^2 + \sum_{i\in cl}\hat{e}_i^2Q_i^2\right), \quad (14)$$

where we have ignored the contribution from lensing shear. Taking the average over a survey field, we have,

$$\langle\sigma^2_{{\rm shape},G}\rangle \simeq \frac{1}{2(n_{fg}+n_{bg})^2} \times \left(\left\langle\sum_{i\in bg}\hat{e}_i^2Q_i^2\right\rangle + \left\langle\sum_{i\in fg}\hat{e}_i^2Q_i^2\right\rangle\right), \quad (15)$$

where we have again assumed that on global average the contribution from the cluster member population is small and have ignored it. Using those expressions, the globally normalized SN defined by equation (7), can be written by

$$SN_G(\boldsymbol{\theta}) = \frac{\mathcal{K}_G(\boldsymbol{\theta})}{\langle\sigma^2_{{\rm shape},G}\rangle^{1/2}} \simeq \frac{\sqrt{2}\sum_{bg}\hat{\gamma}_{t,i}Q_i}{\left(\langle\sum_{bg}\hat{e}_i^2Q_i^2\rangle + \langle\sum_{fg}\hat{e}_i^2Q_i^2\rangle\right)^{1/2}}. \quad (16)$$

Note that in the above expression, there is no contribution from cluster member population. Therefore, the globally normalized estimator is, to a good approximation, free from the dilution effect of the cluster member galaxies.

5.2 Dilution effect of foreground galaxies

Foreground galaxies have two effects on weak lensing peak SNs from clusters. One is to dilute the lensing signal, and the other is to make the shape noise level on mass maps smaller. Below we will first derive relevant expressions for these effects, and evaluate the dilution effect of foreground galaxies using the actual redshift distributions of source galaxies. Then, we will compare it with the real data measured using the secure weak lensing cluster sample.

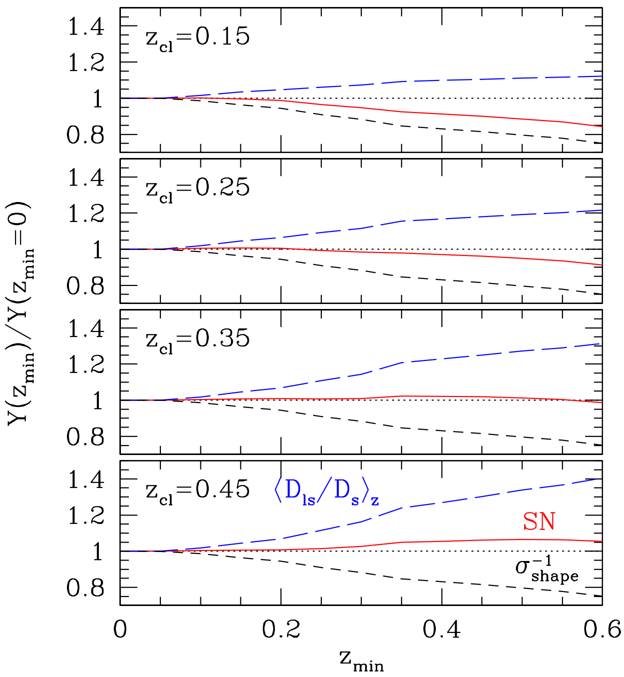

Fig. 5. Shown is dependence of any of $\langle D_{ls}/D_s\rangle_z$ (blue long-dashed lines), $\sigma^{-1}_{\rm shape}$ (black dashed lines) or $SN_{\rm peak}$ (red solid lines) on $z_{\rm min}$. All the quantities (signified by $Y(z_{\rm min})$) are normalized by their values at $z_{\rm min} = 0$. Different panels for different cluster redshifts, z_{cl}, which are denoted in each panel.

Focusing on contributions from foreground and background galaxies, from equation (13), the peak signal can be approximately written by

$$\mathcal{K}_G(\boldsymbol{\theta}) = \frac{1}{n_{fg}+n_{bg}}\sum_{i\in bg}\hat{\gamma}_{t,i}Q_i \propto \frac{n_{bg}\langle\hat{\gamma}_t\rangle_z}{n_{fg}+n_{bg}}, \quad (17)$$

where $\langle\hat{\gamma}_t\rangle_z$ is the source redshift distribution weighted mean tangential shear. Since the source redshift dependence of the tangential shear enters only through the distance ratio, D_{ls}/D_s, we can re-write equation (17) by

$$\mathcal{K}_G(\boldsymbol{\theta}) \propto \left\langle\frac{D_{ls}}{D_s}\right\rangle_z = \frac{\int_{z_{cl}}^{\infty} dz\ n_s(z)D_{ls}(z_{cl},z)/D_s(z)}{\int_0^{\infty} dz\ n_s(z)}, \quad (18)$$

where $n_s(z)$ is the redshift distribution of source galaxies.

In the same manner, from equation (15) we have

$$\langle\sigma^2_{{\rm shape},G}\rangle \propto \frac{(n_{fg}+n_{bg})\langle\hat{e}^2\rangle}{2(n_{fg}+n_{bg})^2} \propto \frac{\langle\hat{e}^2\rangle}{\bar{n}_g}, \quad (19)$$

where we have ignored a possible redshift dependence of $\langle\hat{e}^2\rangle$. This is the well known scaling relation between the shape noise and galaxy number density (Schneider 1996).

The weak lensing peak SN from clusters is related to the source redshift weighted distance ratio and the shape noise via

$$SN \propto \frac{\langle D_{ls}/D_s\rangle_z}{\langle\sigma^2_{{\rm shape},G}\rangle^{1/2}}. \quad (20)$$

Since both the distance ratio and the shape noise depend

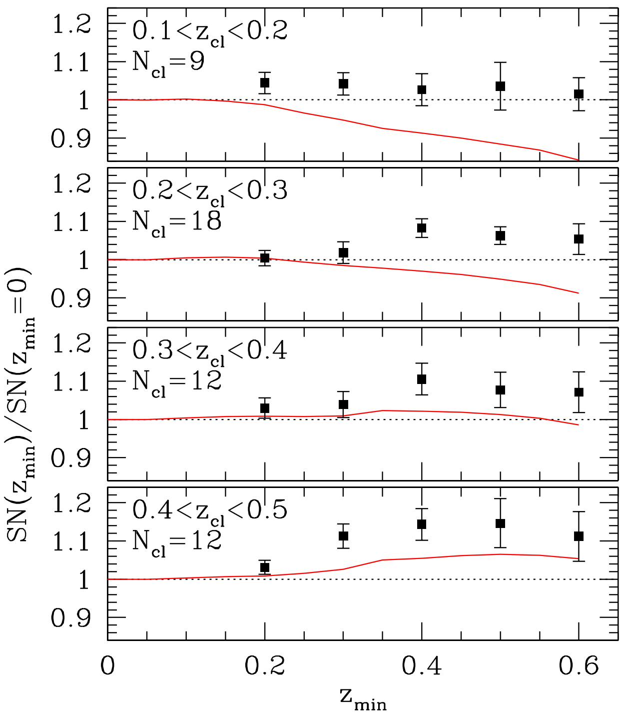

Fig. 6. Shown is the $SN(z_{\rm min})$ of weak lensing secure cluster normalized by its $SN(z_{\rm min}=0)$. Weak lensing secure clusters are divided into four sub-samples based on the cluster redshifts (denoted in panels). The horizontal axis is $z_{\rm min}$ of source galaxy samples. For each sub-sample and each source galaxy sample, the mean and its 1-σ error among the clusters (the number of clusters in each sub-sample is given in each panel) are plotted. For comparison, the red lines show the expected SN ratios plotted in Figure 5 (red lines) for a cluster at a central redshift in respective redshift ranges.

on source galaxy samples, so does the peak SN from a cluster. In our case, the source galaxy selection is characterized by $z_{\rm min}$, and thus we evaluate the dependence of those quantities on $z_{\rm min}$ using the redshift distributions of our source samples defined by equation (2). The results are shown in Figure 5 for cluster redshifts of $z_{cl}=0.15$, 0.25, 0.35, and 0.45. Findings from that figure are as follows: The shape noise, which is not dependent on z_{cl}, monotonically increases with $z_{\rm min}$ as expected. The source redshift weighted distance ratio increases with $z_{\rm min}$. Since a fraction of foreground galaxies is larger for the higher redshift clusters, the higher the cluster redshift, the larger the distance ratio. Those two effects compete; For clusters with redshifts lower than 0.3, their weak lensing peak SN decreases with $z_{\rm min}$. However, for higher redshift clusters, SN stays almost constant or slightly increases with $z_{\rm min}$.

We examine the actual dependence of peak SNs on $z_{\rm min}$ using the weak lensing secure clusters. In doing so, we divide the secure clusters into four sub-samples based on the cluster redshift (to be specific, $0.1<z_{cl}<0.2$, $0.2<z_{cl}<0.3$, $0.3<z_{cl}<0.4$, and $0.4<z_{cl}<0.5$). For each sub-sample, we evaluate the mean of $SN(z_{\rm min})/SN(z_{\rm min}=0)$ and its standard error among sample clusters. The results are shown in Figure 6. We find that the measured ratios of $SN(z_{\rm min})/SN(z_{\rm min}=0)$ is systematically larger than the expectations shown by the red lines (which are same as ones plotted in Figure 5), especially for lower-z clusters ($z_{cl}<0.3$). The reason of this is unclear; a possible cause is the intrinsic alignment of galaxies: Because the major axis of galaxies surrounding a cluster tend to point towards the cluster center due to the intrinsic alignment effects (originating from, e.g., the gravitational tidal stretching, see for a review Joachimi et al. 2015, and references therein), it reduces the peak SN value. Peak SNs of $z_{\rm min}=0$ maps are likely affected by this effect, and consequently they are likely biased low. If this is the case, it accounts for the systematically larger $SN(z_{\rm min})/SN(z_{\rm min}=0)$ found in the measured results, though this argument is rather phenomenological. Aside from this systematic difference, the measured ratios are in reasonable agreement with expectations in their amplitudes and in its increasing trend toward higher-z clusters. From the above findings, we conclude that combining multiple peak catalogs from source samples with different $z_{\rm min}$ can mitigate the dilution effect of foreground galaxies, especially on high-z clusters.

5.3 Impact of the source galaxy deficiency on peak heights

Here we examine the impact on the peak SN from source galaxy deficiency at cluster central regions seen in the stacked galaxy number density profiles shown in Figure 4. We note, however, that deficiency profiles vary greatly from cluster to cluster as is shown in Figure 7.

We use the empirical models of dark matter halo and simple model of the galaxy deficiency profiles, which we describe below. In the presence the source galaxy deficiency, the theoretical expression for the lensing signal from clusters, equation (3), is modified to

$$\mathcal{K}(\boldsymbol{\theta}) = \int d^2\boldsymbol{\phi}\ [1+f_m(\phi)]\gamma_t(\boldsymbol{\phi}:\boldsymbol{\theta})Q(|\boldsymbol{\phi}|), \tag{21}$$

where $f_m(\phi)$ is the source galaxy deficiency profile, for which we adopt the following parametric function,

$$f_m(\phi) = \max\left\{a\left(\frac{\pi}{2}-\tan^{-1}(\frac{\phi}{\phi_0})\right), -1\right\}, \tag{22}$$

where a and ϕ_0 are the amplitude and scale parameters, respectively. We fit the measured deficiency profiles shown in Figure 4 with this function and derive typical values of those parameters that we take in the following analysis. We consider three models of $f_m(\phi)$ shown in the top-panel of Figure 8: The model with $a=-0.25$ mimics the stacked

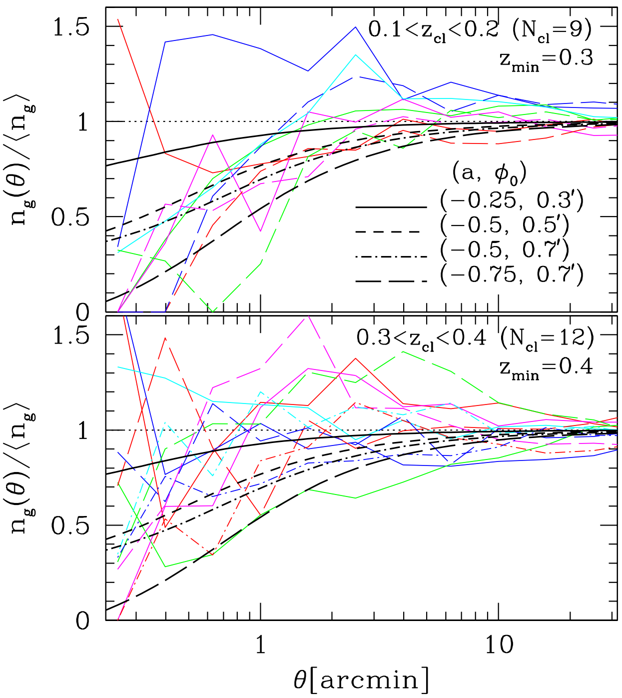

Fig. 7. Thin colored lines show azimuthally averaged galaxy number density normalized by the mean number density as a function of the angular separation from peak positions. Each colored line is for an individual cluster. Sub-samples of weak lensing secure clusters are shown. The upper/lower panel is for the clusters at $0.1 < z_{cl} < 0.2/0.3 < z_{cl} < 0.4$ with the source galaxy sample of $z_{\rm min} = 0.3/0.4$. The thick black lines show the parametric model, equation (22) but plotted is $[1 + f_m(\theta)]$, for four sets of parameters denoted in the upper panel.

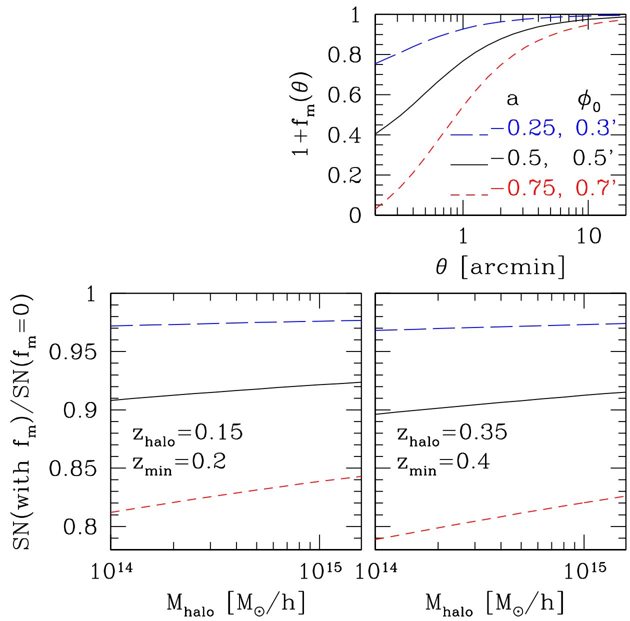

Fig. 8. *Top-panel*: Three models of the source galaxy deficiency profile are shown. See equation (22) for the functional form of the model. *Bottom-panels*: Shown is ratios between expected peak SNs of an NFW halo with and without taking the source galaxy deficiency into account as a function of halo mass (the virial mass is taken here). The left-panel is for the case $z_{\rm halo} = 0.15$ with the galaxy redshift distribution taken from the source sample with $z_{\rm min} = 0.2$, whereas the right-panel is for $z_{\rm halo} = 0.35$ with $z_{\rm min} = 0.4$. Different lines are for different deficiency models shown in the top-panel.

deficiency profile of a case $0.3 < z_{cl} < 0.4$ with $z_{\rm min} > z_{cl}$, and the model with $a = -0.5$ mimics ones of $0.1 < z_{cl} < 0.2$ (see Figure 4), whereas the model with $a = -0.75$ represents extreme cases from individual clusters shown in Figure 7. Since details of the models needed to compute equation (21) are described in Hamana et al. (2012), here we summarize the main ingredients and relevant references:

- Dark matter halos of clusters are modeled by the truncated NFW model (Baltz et al. 2009) with the mass-concentration relation by Macciò et al. (2008) and Duffy et al. (2008).
- Redshift distributions of source galaxies of our source samples are estimated by equation (2), which are dependent on $z_{\rm min}$, and are presented in Figure 1.

Results are presented in Figure 8. Note, however, that since the deficiency model is a crude approximation and halo mass dependence of the source deficiency is not taken into account, the results should be considered as a rough estimate of the impact of source deficiency on a peak SN. In the bottom-panels, ratios between expected peak SNs with and without taking the source deficiency into account as a function of halo mass are shown for three deficiency models presented in the top-panel. The left-panel is for the case $z_{\rm halo} = 0.15$, whereas the right-panel is for $z_{\rm halo} = 0.35$. We find that in both the cases, the suppression of SN due to the source deficiency is 2–5 percent for models with $a = -0.25$, 8–10 percent for $a = -0.5$ and 16–20 percent for the extreme case of $a = -0.75$. We thus conclude that a typical impact of source deficiency on a peak SN is a suppression of a few to ~ 10 percent. However it can be ~ 20 percent for individual cases. It is also seen in the Figure that for a given source deficiency model, the suppression decreases with increasing halo mass. The reason for this is that a relative contribution to a peak SN from galaxies within a fixed aperture is smaller for more massive halos.

6 Summary and discussions

We have presented a weak lensing cluster search using HSC first-year data. We generated six samples of source galaxies with different $z_{\rm min}$-cuts (we took $z_{\rm min} = 0$, 0.2, 0.3, 0.4, 0.5 and 0.6), and made weak lensing mass maps for each source sample from which we searched for high peaks. From each source sample, we detected a sample of 68–75 weak lensing peaks with $SN \geq 5$. We compiled the six peak samples into a sample of merged peaks. We obtained a sample of

124 weak lensing merged peaks with $SN_{\max} \geq 5$ which are candidates of clusters of galaxies.

We cross-matched our peak sample with CAMIRA-HSC clusters (Oguri et al. 2018) to identify cluster counterparts of the peaks. We found that 107 out of 124 merged peaks have matched CAMIRA-HSC clusters within 5 arcmin from the peak positions. Among the 107 matched peaks, 25 peaks have multiple matches, which might be generated by line-of-sight projections of multiple clusters. Among the remaining 82 peaks matching with a single CAMIRA-HSC cluster, 64 peaks have CAMIRA-HSC cluster counterparts within 2 arcmin from peak positions. We confirmed by visual inspection of HSC images and found that, for all 64 peaks, there exist good correlations between weak lensing mass over-densities and galaxy concentrations. We thus defined those peaks as the sample of *weak lensing secure clusters*, and used them to examine the dilution effects on our weak lensing peak finding.

We have paid particular attention to the dilution effect of cluster member and foreground galaxies on weak lensing peak SNs, and have adopted two means to mitigate its impact, namely the globally normalized estimator [equations (5), and (6)], and the source galaxy selection with different $z_{\min}$-cuts using the full probability distribution function of galaxy photo-zs.

We have demonstrated, using the simple model of galaxy populations introduced in Section 5.1, that the peak SN defined by the globally normalized estimators is, to a good approximation, not affected by the dilution effect of the cluster member galaxies. This is in marked contract to the locally normalized SN which is indeed affected by the cluster member galaxies as demonstrated in Appendix 4. We compared the peak heights of the globally normalized SN_G with ones of the locally normalized SN_L using our weak lensing mass maps, and found that for the peak samples with $SN_G \geq 5$, SN_Gs are, on average, about 10 percent larger than the corresponding SN_Ls.

In Section 5.2, we have examined the dilution effect of foreground galaxies and have demonstrated the ability of our source galaxy selection to mitigate it. We used the probability distribution function of photo-z, and adopted *P-cut* method (Oguri 2014) to remove galaxies at $z < z_{\min}$ which are foreground galaxies of clusters at $z_{cl} > z_{\min}$. This galaxy selection has two competing influences on weak lensing peak SNs from clusters: One is to reduce the dilution effect of foreground galaxies, and the other is to increase the shape noise level as the $z_{\min}$-cut reduces the number density of source galaxies. We examined the expected impact on peak SN heights from those two factors using the estimated redshift distribution of the source samples, and found that for high/low-z clusters ($z \gtrsim 0.3/z \lesssim 0.2$), the former/latter is more effective than the latter/former, leading to a gain/decline in peak SNs with increasing $z_{\min}$.

We examined the actual dependence of peak SNs on the source selection using the weak lensing secure clusters. We measured the ratios of $SN(z_{\min})/SN(z_{\min}=0)$ for four sub-samples of secure clusters divided based on the cluster redshift (shown in Figure 6). We found that the measured results were in reasonable agreement with the expectations in their amplitudes and in their increasing trend toward higher-z clusters, except for the systematic offset of about +5 to +10 percent which could be due to the intrinsic alignment of cluster neighbor galaxies. From the above findings, along with the fact that the number of merged peak sample (124 for $SN_{\max} \geq 5$) is nearly twice of the numbers from individual source samples (68–75 for $SN \geq 5$), we conclude that combining multiple peak samples from source samples with different $z_{\min}$ indeed improve the efficiency of weak lensing cluster search, especially for high-z clusters.

We have also examined the effect of source galaxy deficiency on weak lensing peak heights. The source deficiency was clearly observed in stacked galaxy number density profiles of secure clusters at cluster central regions for the cluster sample of $0.1 < z_{cl} < 0.2$ and for the other samples with $z_{\min} > z_{cl}$ (Figure 4). This can be due to the masking effect of bright cluster galaxies and/or the lensing magnification effect. Using a simple model consisting of spatial profiles of dark matter halo density and source deficiency, we make predictions for the source deficiency effect on the peak SN. We found that for realistic models of source deficiency, a peak SN is suppressed by a few to ~ 10 percent.

Since we have focused on the dilution effect, there are some important tasks/issues related to weak lensing cluster search which have not been examined in this paper: The three major matters among others are:

1. The purity of the sample of 124 weak lensing cluster candidates: For each of 64 weak lensing secure clusters, we have found a good correlation between weak lensing mass over-density and galaxy concentration, and have concluded that those weak lensing signals have a physical relationship with the counterpart CAMIRA-HSC cluster. The remaining 60 peaks fall into the following three categories:
(a) 18 cases: peaks matching with a single CAMIRA-HSC clusters but their separations are larger than 2 arcmin. Physical connections between those weak lensing mass over-densities and clusters are not clear, which are a subject of a future study.
(b) 25 cases: peaks having multiple CAMIRA-HSC clus-

ters within 5 arcmin. In 23 out of the 25 cases, matched clusters of the same peak are separated in the redshift direction by $\Delta z > 0.1$. Thus those peaks are likely affected by line-of-sight projections of physically unrelated clusters, though detail investigations of each peak are required to reveal their real nature.

(c) 17 cases: Peaks have no matched CAMIRA-HSC cluster, for which we searched for possible counterpart clusters in a known cluster database taken from a compilation by `NASA/IPAC Extragalactic Database` (NED[5]). The results are presented in Appendix 1.1. In 10 out of 17 peaks, possible counterpart clusters are found (see Table 4). In Figure 9, we show HSC riz composite images of the remaining 7 peaks (that have no counterpart cluster found), in which good correlations between the weak lensing mass over-density and galaxy concentration are seen in some of those systems. Clearly, the above information is not enough to evaluate the purity of our sample; further followup studies combining information from other wavelength data (for example, X-ray and Sunyaev-Zel'dovich effect) are required.

2. Weak lensing mass estimate of our cluster candidates: Although cluster mass derived from weak lensing analysis can add valuable information to our sample, an accurate determination of cluster redshift as well as carefully taking account of line-of-sight projections of uncorrelated objects are required to estimate weak lensing mass accurately. We have derived weak lensing cluster masses only for weak lensing secure clusters which have good correlations between the weak lensing mass peak and galaxy over-density (see Appendix 3). Since the remaining weak lensing peaks have either multiple CAMIRA-HSC cluster counterparts or a less correlated/no CAMIRA-HSC cluster counterpart, further detailed studies of individual systems are needed to derive their cluster masses, which we leave for a future study.
3. Masking effect of bright cluster galaxies and lensing magnification effect on weak lensing peak finding: As we discussed in the above, we have seen an observational indication of those effects as the deficiency of source galaxies at cluster central regions, and have examined their impact on the peak SN in Section 5.3. Since those effects are unavoidable in weak lensing cluster search, a further detail study of those effects is important for cosmological applications of weak lensing selected clusters. It is, however, beyond the scope of this paper, and we leave it for a future study.

[5] http://ned.ipac.caltech.edu/

Weak lensing mass maps contain a wealth of cosmological information beyond those obtained by analyses of the cosmic shear power spectrum or two-point correlation function (see, for example, Dietrich & Hartlap 2010; Yang et al. 2011; Petri et al. 2013; Shirasaki et al. 2017). However, in this study, we showed that if a source galaxy sample is selected by, for example, a simple magnitude-cut, the dilution effects may alter SNs of high peaks in a non-negligible amount, and thus may modify statistical properties of weak lensing mass maps. Therefore, when one uses weak lensing mass maps for a cosmological application, the dilution and the source deficiency effects must be taken into account. We note that the effects are dependent on the source sample that one takes, and thus should be examined on a case-by-case basis. At the same time, developing source galaxy selection methods that can mitigate the dilution effects is another important subject in that research field.

Acknowledgments

We would like to thank Masamune Oguri for useful comments on an earlier manuscript, and Satoshi Miyazaki for useful discussions. We would like to thank Nick Kaiser for making the software `imcat` publicly available, and `ds9` developers for `ds9` publicly available. We have heavily used those softwares in this study. We would like to thank HSC data analysis software team for their effort to develop data processing software suite, and HSC data archive team for their effort to build and to maintain the HSC data archive system.

This work was supported in part by JSPS KAKENHI Grant Number JP17K05457. MS is supported by JSPS Overseas Research Fellowships.

Data analysis were in part carried out on PC cluster at Center for Computational Astrophysics, National Astronomical Observatory of Japan. Numerical computations were in part carried out on Cray XC30 and XC50 at Center for Computational Astrophysics, National Astronomical Observatory of Japan, and also on Cray XC40 at YITP in Kyoto University.

The Hyper Suprime-Cam (HSC) collaboration includes the astronomical communities of Japan and Taiwan, and Princeton University. The HSC instrumentation and software were developed by the National Astronomical Observatory of Japan (NAOJ), the Kavli Institute for the Physics and Mathematics of the Universe (Kavli IPMU), the University of Tokyo, the High Energy Accelerator Research Organization (KEK), the Academia Sinica Institute for Astronomy and Astrophysics in Taiwan (ASIAA), and Princeton University. Funding was contributed by the FIRST program from Japanese Cabinet Office, the Ministry of Education, Culture, Sports, Science and Technology (MEXT), the Japan Society for the Promotion of Science (JSPS), Japan Science and Technology Agency (JST), the Toray Science Foundation, NAOJ, Kavli IPMU, KEK, ASIAA, and Princeton University. This paper makes use of software developed for the Large Synoptic Survey Telescope.

We thank the LSST Project for making their code available as free software at `http://dm.lsst.org`

The Pan-STARRS1 Surveys (PS1) have been made possible through contributions of the Institute for Astronomy, the University of Hawaii, the Pan-STARRS Project Office, the Max-Planck Society and its participating institutes, the Max Planck Institute for Astronomy, Heidelberg and the Max Planck Institute for Extraterrestrial Physics, Garching, The Johns Hopkins University, Durham University, the University of Edinburgh, Queen's University Belfast, the Harvard-Smithsonian Center for Astrophysics, the Las Cumbres Observatory Global Telescope Network Incorporated, the National Central University of Taiwan, the Space Telescope Science Institute, the National Aeronautics and Space Administration under Grant No. NNX08AR22G issued through the Planetary Science Division of the NASA Science Mission Directorate, the National Science Foundation under Grant No. AST-1238877, the University of Maryland, and Eotvos Lorand University (ELTE) and the Los Alamos National Laboratory.

Based in part on data collected at the Subaru Telescope and retrieved from the HSC data archive system, which is operated by Subaru Telescope and Astronomy Data Center at National Astronomical Observatory of Japan.

References

Abell, G. O., Corwin, Harold G., J., & Olowin, R. P. 1989, ApJS, 70, 1
Adami, C., Giles, P., Koulouridis, E., et al. 2018, A&A, 620, A5
Aihara, H., Armstrong, R., Bickerton, S., et al. 2018a, PASJ, 70, S8
Aihara, H., Arimoto, N., Armstrong, R., et al. 2018b, PASJ, 70, S4
Aihara, H., AlSayyad, Y., Ando, M., et al. 2019, PASJ, 106
Allen, S. W., Evrard, A. E., & Mantz, A. B. 2011, ARA&A, 49, 409
Baltz, E. A., Marshall, P., & Oguri, M. 2009, J. Cosmology Astropart. Phys., 1, 15
Bartelmann, M., & Schneider, P. 2001, Phys. Rep., 340, 291
Bosch, J., Armstrong, R., Bickerton, S., et al. 2018, PASJ, 70, S5
Broadhurst, T., Takada, M., Umetsu, K., et al. 2005, ApJ, 619, L143
Chiu, I.-N., Umetsu, K., Murata, R., Medezinski, E., & Oguri, M. 2019, arXiv e-prints, arXiv:1909.02042
Clerc, N., Adami, C., Lieu, M., et al. 2014, MNRAS, 444, 2723
Dietrich, J. P., & Hartlap, J. 2010, MNRAS, 402, 1049
Duffy, A. R., Schaye, J., Kay, S. T., & Dalla Vecchia, C. 2008, MNRAS, 390, L64
Durret, F., Adami, C., Cappi, A., et al. 2011, A&A, 535, A65
Farrens, S., Abdalla, F. B., Cypriano, E. S., Sabiu, C., & Blake, C. 2011, MNRAS, 417, 1402
Furusawa, H., Koike, M., Takata, T., et al. 2018, PASJ, 70, S3
Goto, T., Sekiguchi, M., Nichol, R. C., et al. 2002, AJ, 123, 1807
Gruen, D., Seitz, S., Becker, M. R., Friedrich, O., & Mana, A. 2015, MNRAS, 449, 4264
Hamana, T., Oguri, M., Shirasaki, M., & Sato, M. 2012, MNRAS, 425, 2287
Hamana, T., Sakurai, J., Koike, M., & Miller, L. 2015, PASJ, 67, 34
Hamana, T., Takada, M., & Yoshida, N. 2004, MNRAS, 350, 893
Hao, J., McKay, T. A., Koester, B. P., et al. 2010, ApJS, 191, 254
Heymans, C., Van Waerbeke, L., Miller, L., et al. 2012, MNRAS, 427, 146
Hikage, C., Oguri, M., Hamana, T., et al. 2019, PASJ, 71, 43
Hinshaw, G., Larson, D., Komatsu, E., et al. 2013, ApJS, 208, 19
Hirata, C., & Seljak, U. 2003, MNRAS, 343, 459
Hoekstra, H. 2003, MNRAS, 339, 1155
—. 2007, MNRAS, 379, 317
Ivezić, Ž., Kahn, S. M., Tyson, J. A., et al. 2019, ApJ, 873, 111
Joachimi, B., Cacciato, M., Kitching, T. D., et al. 2015, Space Sci. Rev., 193, 1
Kaiser, N. 1995, ApJ, 439, L1
Kawanomoto, S., Uraguchi, F., Komiyama, Y., et al. 2018, PASJ, 70, 66
Koester, B. P., McKay, T. A., Annis, J., et al. 2007, ApJ, 660, 239
Komiyama, Y., Obuchi, Y., Nakaya, H., et al. 2018, PASJ, 70, S2
Kravtsov, A. V., & Borgani, S. 2012, ARA&A, 50, 353
Laureijs, R., Gondoin, P., Duvet, L., et al. 2012, Society of Photo-Optical Instrumentation Engineers (SPIE) Conference Series, Vol. 8442, Euclid: ESA's mission to map the geometry of the dark universe, 84420T
Limousin, M., Richard, J., Jullo, E., et al. 2007, ApJ, 668, 643
Macciò, A. V., Dutton, A. A., & van den Bosch, F. C. 2008, MNRAS, 391, 1940
Mandelbaum, R., Miyatake, H., Hamana, T., et al. 2018a, PASJ, 70, S25
Mandelbaum, R., Lanusse, F., Leauthaud, A., et al. 2018b, MNRAS, 481, 3170
Medezinski, E., Broadhurst, T., Umetsu, K., et al. 2007, ApJ, 663, 717
Medezinski, E., Oguri, M., Nishizawa, A. J., et al. 2018, PASJ, 70, 30
Miyatake, H., Battaglia, N., Hilton, M., et al. 2019, ApJ, 875, 63
Miyazaki, S., Hamana, T., Shimasaku, K., et al. 2002, ApJ, 580, L97
Miyazaki, S., Oguri, M., Hamana, T., et al. 2018a, PASJ, 70, S27
Miyazaki, S., Komiyama, Y., Kawanomoto, S., et al. 2018b, PASJ, 70, S1
Navarro, J. F., Frenk, C. S., & White, S. D. M. 1997, ApJ, 490, 493
Oguri, M. 2014, MNRAS, 444, 147
Oguri, M., Lin, Y.-T., Lin, S.-C., et al. 2018, PASJ, 70, S20
Okabe, N., Takada, M., Umetsu, K., Futamase, T., & Smith, G. P. 2010, PASJ, 62, 811
Pacaud, F., Clerc, N., Giles, P. A., et al. 2016, A&A, 592, A2
Petri, A., Haiman, Z., Hui, L., May, M., & Kratochvil, J. M. 2013, Phys. Rev. D, 88, 123002
Pierre, M., Pacaud, F., Adami, C., et al. 2016, A&A, 592, A1

Piffaretti, R., Arnaud, M., Pratt, G. W., Pointecouteau, E., & Melin, J. B. 2011, A&A, 534, A109
Planck Collaboration, Aghanim, N., Akrami, Y., et al. 2018, ArXiv e-prints, arXiv:1807.06209
Pratt, G. W., Arnaud, M., Biviano, A., et al. 2019, Space Sci. Rev., 215, 25
Racca, G., Laureijs, R., & Mellier, Y. 2018, in 42nd COSPAR Scientific Assembly, Vol. 42, E1.16–3–18
Schmidt, F., & Rozo, E. 2011, ApJ, 735, 119
Schneider, P. 1996, MNRAS, 283, 837
Shirasaki, M., Nishimichi, T., Li, B., & Higuchi, Y. 2017, MNRAS, 466, 2402
Tanaka, M., Coupon, J., Hsieh, B.-C., et al. 2018, PASJ, 70, S9
Umetsu, K., & Broadhurst, T. 2008, ApJ, 684, 177
Umetsu, K., Sereno, M., Lieu, M., et al. 2020, ApJ, 890, 148
van Waerbeke, L. 2000, MNRAS, 313, 524
Wen, Z. L., & Han, J. L. 2011, ApJ, 734, 68
Wen, Z. L., Han, J. L., & Liu, F. S. 2009, ApJS, 183, 197
Yang, X., Kratochvil, J. M., Wang, S., et al. 2011, Phys. Rev. D, 84, 043529

Appendix 1 Cross-matching with selected cluster catalogs

A.1.1 Cluster counterparts of weak lensing peaks with no CAMIRA-HSC cluster counterpart

Among 124 weak lensing merged peaks, 17 peaks have no CAMIRA-HSC cluster counterparts within a 5 arcmin radius from the peak positions. However, note that one of them, HWL16a-121, is a known cluster (Abell 2457) at $z = 0.059$ which is outside the redshift coverage of CAMIRA algorithm (Oguri et al. 2018).

We search for cluster counterparts of those peaks in a known cluster database taken from a compilation by `NASA/IPAC Extragalactic Database` (NED). Clusters matched within 5 arcmin radius from the peak positions are summarized in Table 4. In 10 out of 17 peaks, possible counterpart clusters are found. For the remaining 7 peaks, we present HSC riz-band composite images in Figure 9 [panels (a)–(g)]. In that Figure, we find apparent galaxy concentrations near the weak lensing peaks of HWL16a-001, 011, 096, 118, and 122. It follows from this that those peaks are not necessarily false signals, but undiscovered counterpart clusters may exist.

In summary, combining results of cross-matching with CAMIRA-HSC cluster catalog and with known cluster database, we have found possible counterpart clusters for 117 out of 124 weak lensing peaks. However, since our matching is based on a simple positional correlation, some of matches can be chance projections. Future followup studies of individual peaks on a case-by-case basis are required to reveal physical connections between weak lensing peaks and matched clusters.

A.1.2 Cross-matching with XXL clusters

Adami et al. (2018) have presented a sample of 365 clusters of galaxies detected in the XXL Survey, which is a wide-field and deep X-ray imaging survey conducted with *XMM-Newton* (Pierre et al. 2016). The XXL survey consists of two survey fields, each covering ~ 25 deg^2 area, and its north field (XXL-N) largely overlaps with our XMM field (see Figure 1 of Umetsu et al. 2020). Since the selection function of XXL clusters with respect to the cluster mass and redshift well covers that of our clusters (see, e.g., Fig 12 of Miyazaki et al. 2018a), the XXL cluster sample provides good reference data to test the completeness of our weak lensing clusters.

Among 23 weak lensing merged peaks in XMM field (HWL16a-001–023), 14 peaks are located on the XXL survey footprints (see Figure 1 of Pacaud et al. 2016). 11 out of 14 peaks have XXL cluster counterparts (see Table 3). The peaks with no XXL cluster counterpart are HWL16a-015, 018, and 019, for which brief descriptions are given below, though future detail investigations of each peak are required to reveal their real nature:

- HWL16a-015 matches with XLSSC 074 (Clerc et al. 2014) which is not contained in XXL 365 cluster sample (Adami et al. 2018). There are three known clusters within 5 arcmin from the peak position; see Appendix 1.1 for details.
- HWL16a-018 has no CAMIRA-HSC cluster counterpart. There are four known clusters within 5 arcmin from the peak position; see Appendix 1.1 for details.
- HWL16a-019 has one CAMIRA-HSC cluster counterpart (CAMIRA-ID 388, $z_{cl} = 1.011$), but the separation between them is 5.0 arcmin. Therefore the physical connection between the weak lensing peak and CAMIRA-HSC 388 is uncertain. There is one known cluster, CFHTLS W1-2587 ($z_{cl} = 0.30$, Durret et al. 2011), with the angular separation of 1.2 arcmin.

We note that both HWL16a-021 and HWL16a-022 match with the same XXL cluster, XLSSC 151 at $z = 0.189$. Also, both peaks match with the same CAMIRA-HSC cluster (CAMIRA-ID 355, the estimated redshift of $z = 0.276$). In fact, those two are a close pair of peaks with their separation of ~ 3 arcmin (see Figure 9 (i)), though they are identified as two individual peaks under our peak identification criteria (described in section 3.3). It is seen in Figure 9 (i) that the X-ray cluster XLSSC 151 is at the peak position of HWL16a-021, whereas CAMIRA-HSC cluster 355 matches better with HWL16a-022. Considering the difference in redshifts of those two clusters, it is likely that the twin peaks of the weak lensing SN map arise from a chance line-of-sight projection of two physically sepa-

(a) HWL16a-001

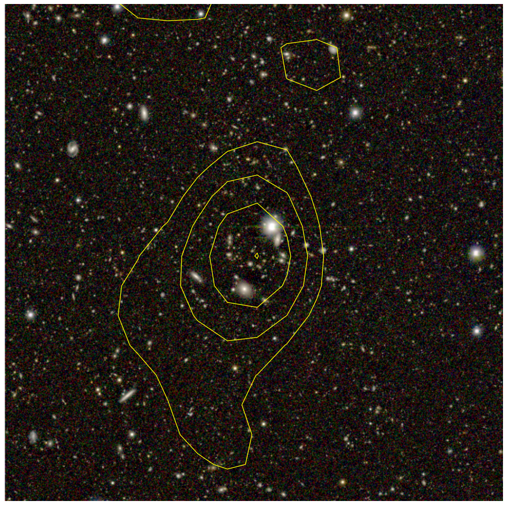

(b) HWL16a-011

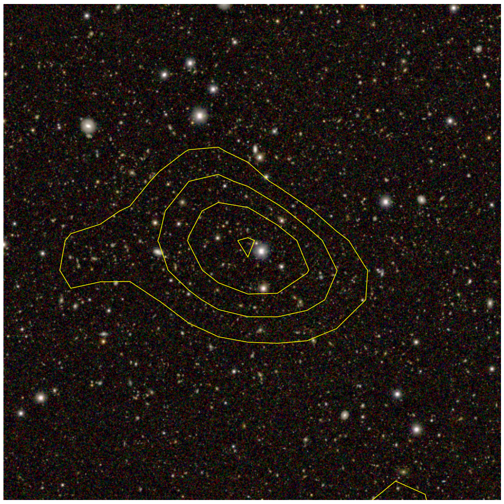

(c) HWL16a-061

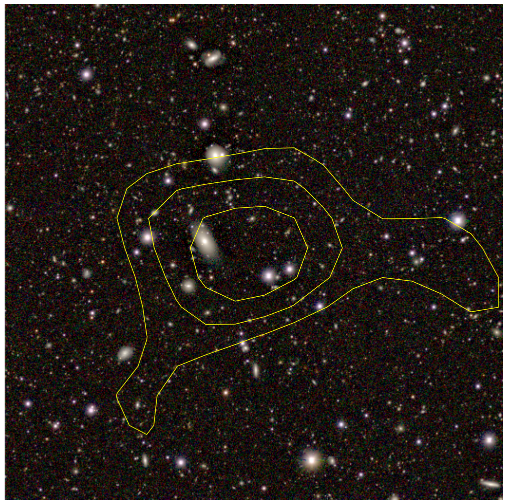

(d) HWL16a-096

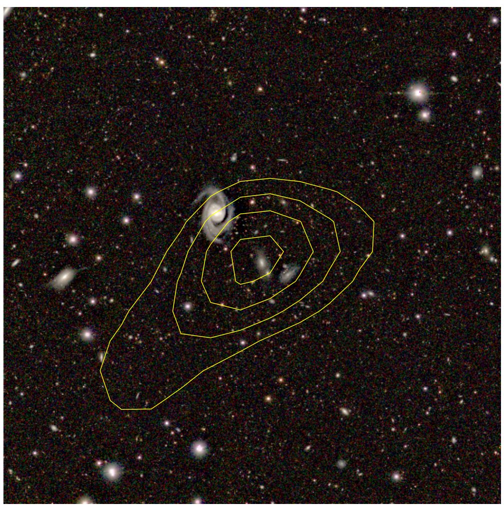

(e) HWL16a-118

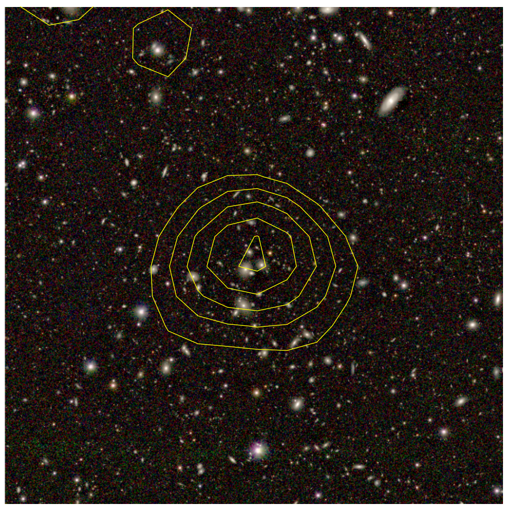

(f) HWL16a-122

Fig. 9. HSC riz-band composite images with a side length of 10 arcmin. The yellow contour shows the weak lensing SN, the contour lines start from $SN = 2$ with the interval of 1. The first 7 panels [(a)–(g)] show weak lensing peaks having no CAMIRA-HSC counterpart being matched within 5 arcmin radius from the peak position. The last 7 panels [(h)–(n)] show systems of neighboring peaks having a common CAMIRA-HSC counterpart. Positions of CAMIRA-HSC cluster (based on HSC S16A data with updated star mask, Oguri et al. 2018) and XXL clusters (Adami et al. 2018) are marked with plus symbols.

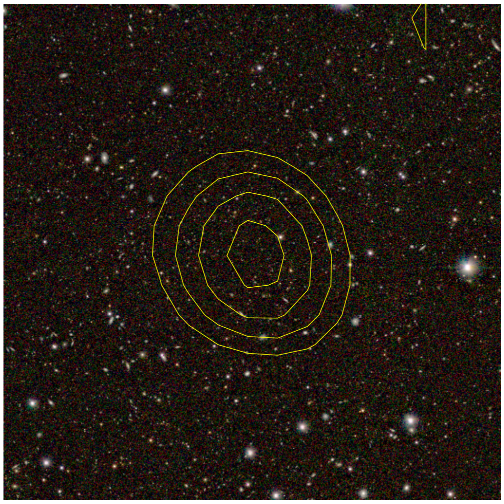

(g) HWL16a-123

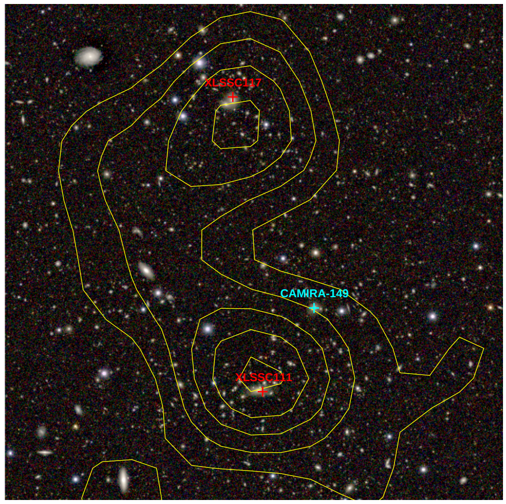

(h) HWL16a-007 (lower peak), and 008 (upper peak)

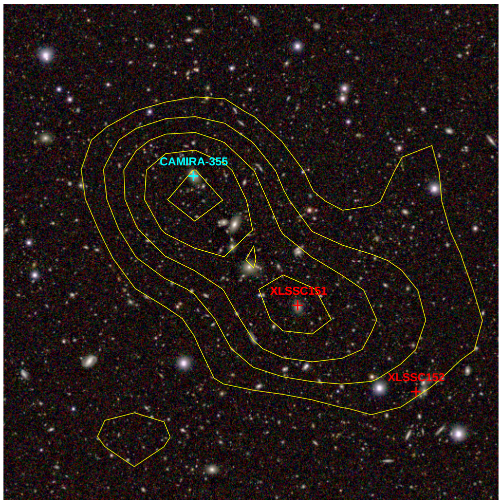

(i) HWL16a-021 (lower peak), and 022 (upper peak)

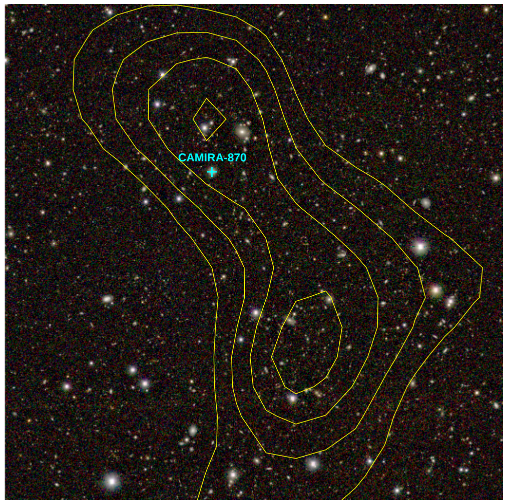

(j) HWL16a-044 (lower peak), and 045 (upper peak)

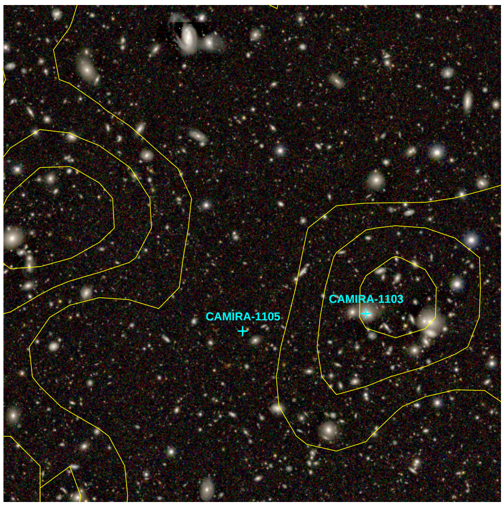

(k) HWL16a-062 (right-peak), and 063 (left peak)

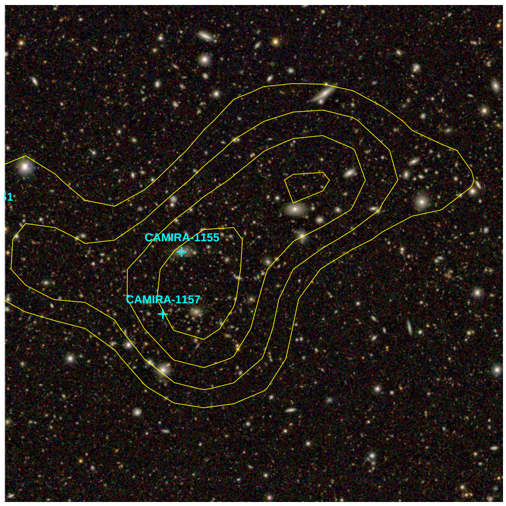

(l) HWL16a-068 (upper peak), and 069 (lower peak)

Fig. 9. (Continued)

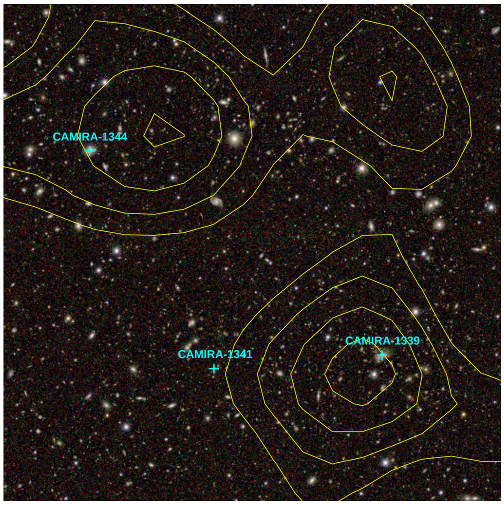

(m) HWL16a-085 (lower peak), and 086 (upper-left peak)

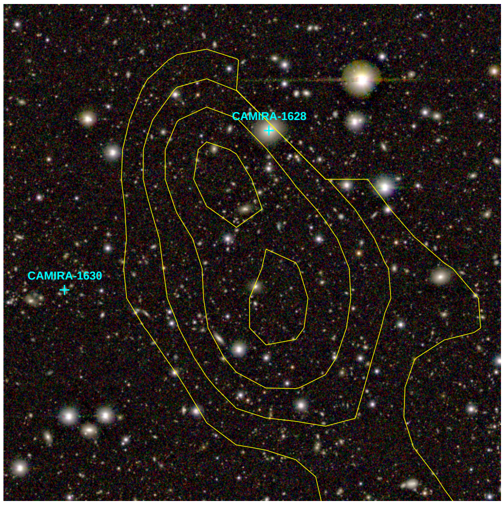

(n) HWL16a-105 (lower peak), and 106 (upper peak)

Fig. 9. (Continued)

rated clusters. If this is the case, HWL16a-022 is another weak lensing peak having no XXL cluster counterpart.

A.1.3 Cross-matching with weak lensing peaks in Miyazaki et al. (2018a)

Miyazaki et al. (2018a, M18 hereafter) presented a sample of weak lensing peaks detected in mass maps constructed from the HSC first-year shape catalog (Mandelbaum et al. 2018a) that we also used in this study. Although their method of weak lensing mass map construction is very similar to that of this study, differences in source galaxy selection and criteria of peak identification result in different peak samples. Their peak sample contains 65 peaks with $SN > 4.7$. We cross-match their peaks with our extended-sample (peaks with $SN \geq 4$ are included) by their peak positions to a tolerance of $\theta_G = 1.5$ arcmin. Among their 65 peaks, 51 peaks match with our final merged peaks ($SN \geq 5$, see Table 3). The remaining 14 peaks fall into the following five categories:

1. [M18 rank 51]: A corresponding peak exists in our final merged sample (HWL16a-054), but their separation is 2.6 arcmin which exceeds the tolerance length.
2. [M18 rank 49, 55, and 60]: A matched peak exists in our extended-sample with $5 > SN_{\max} \geq 4$, but its $SN_{\max}$ is below our threshold.
3. [M18 rank 7, 27, 31, 41 and 43]: A corresponding peak exists in our extended-sample with $SN_{\max} \geq 4$, but is located in the edge-region.
4. [M18 rank 37 and 38]: No corresponding peak exists in our extended-sample. Note that both the peaks are located in our edge-region.
5. [M18 rank 15, 45 and 46]: Those peaks are located in our masked-regions where we have not performed weak lensing analysis.

In summary, among 65 peaks in M18 sample, all the 55 peaks located in our data-regions have counterpart peaks in our extended-sample (including M18 rank 51–HWL16a-054).

Appendix 2 Systems of neighboring weak lensing peaks

In weak lensing mass maps, there are systems of neighboring peaks; those are either two isolated clusters or one cluster having a significant substructure or under a merging process. Distinguishing clusters' dynamical states with only the weak lensing information is practically impossible. Nevertheless, we have adopted a simple criterion that neighboring peaks with their separation larger than $\sqrt{2} \times \theta_G \simeq 2.1$ arcmin are regarded as two isolated peaks (see Section 3.3). Consequently, there are systems of neighboring peaks, whose dynamical states are ambiguous, in our final peak catalog (Table 3).

Here we describe those systems of neighboring peaks having a common CAMIRA-HSC cluster within 5 arcmin from both the peaks. There are seven such systems, whose HSC riz composite images are shown in Figure 9 [panels (h)–(n)]. Below we give short descriptions of them:

- HWL16a-007 and 008 [Figure 9 (h)]: Although both peaks have a common CAMIRA-HSC counterpart (ID-149, $z_{cl} = 0.287$), they match with the different XXL clusters, XLSSC 111 ($z = 0.299$) and XLSSC 117 ($z = 0.300$). Thus those are likely two isolated clusters at very close redshifts.

- HWL16a-021 and 022 [Figure 9 (i)]: See Appendix 1.2.
- HWL16a-044 and 045 [Figure 9 (j)]: CAMIRA-HSC cluster (ID-870, $z_{cl} = 0.260$) matches better with HWL16a-045. Not enough information is available to infer the physical connection between those two peaks.
- HWL16a-062 and 063 [Figure 9 (k)]: CAMIRA-HSC cluster (ID-1103, $z_{cl} = 0.144$) matches better with HWL16a-062. Another cluster (ID-1105, $z_{cl} = 1.105$) is probably a non-related high-z cluster as no associated lensing signal appears. Other than that, no known clusters can be associated with it. However, a good correlation between HWL16a-063 and an apparent concentration of bright galaxies is clearly seen.
- HWL16a-068 and 069 [Figure 9 (l)]: Both the peaks match with CAMIRA-HSC clusters (ID-1155, $z_{cl} = 0.322$) and (ID-1157, $z_{cl} = 0.515$). Because of the difference in the cluster redshifts, the lensing signals likely originate from line-of-sight projections of the two clusters at different redshifts.
- HWL16a-085 and 086 [Figure 9 (m)]: HWL16a-085 matches better with CAMIRA-HSC cluster (ID-1339, $z_{cl} = 0.536$), whereas HWL16a-086 matches better with CAMIRA-HSC cluster (ID-1344, $z_{cl} = 0.149$). Another cluster (ID-1341, $z_{cl} = 0.884$) is probably a non-related high-z cluster, as no associated lensing signal appears. Thus the two peaks originate from two isolated clusters.
- HWL16a-105 and 106 [Figure 9 (n)]: CAMIRA-HSC cluster (ID-1628, $z_{cl} = 0.100$) matches better with HWL16a-106. No apparent lensing signal associated with another cluster (ID-1680, $z_{cl} = 0.357$) appears. Not enough information is available to infer the physical connection between those two peaks.

Appendix 3 Cluster mass estimate

Here we present the method and results of cluster mass estimate of the weak lensing peaks that meet the following two conditions:

1. Those peaks should be classified as weak lensing secure clusters (see Section 4) to ensure the presence of a secure cluster counterpart, and to avoid systems with line-of-sight projection. The latter is required as our cluster model (described below) assumes a single dark matter halo.
2. Cluster redshift should be lower than 0.7 to have a sufficient number density of background galaxies for the measurement of weak lensing shear profile (described below).

61 weak lensing secure clusters meet those conditions (see Table 5).

We derive cluster masses by fitting the NFW model (Navarro et al. 1997) to measured weak lensing shear profiles based on the standard likelihood analysis. We employ the weak lensing mass estimate procedure of Umetsu et al. (2020) who used the same HSC first-year shear catalog as one used in this study, allowing us to closely follow their procedure. Since details of the procedure are described in Umetsu et al. (2020, and see the references therein), below we describe those aspects that are directly relevant to this study.

For each cluster, we select background galaxies using the P-cut method (see Section 3.4 of Umetsu et al. 2020, and see also Medezinski et al. 2018) with the cluster redshift taken from the estimated redshift of matched CAMIRA-HSC clusters[6], and we measure the azimuthally averaged tangential shear (γ_t) which relates to the excess surface mass density $\Delta\Sigma$ as (Kaiser 1995)

$$\gamma_t(R) = \frac{\bar{\Sigma}(<R) - \Sigma(R)}{\Sigma_{cr}(z_{cl}, z_s)} \equiv \frac{\Delta\Sigma(R)}{\Sigma_{cr}(z_{cl}, z_s)}, \tag{A1}$$

where $\Sigma(R)$ is the azimuthally averaged surface mass density at R, $\bar{\Sigma}(<R)$ denotes the average surface mass density interior to R, and $\Sigma_{cr}(z_{cl}, z_s)$ is the critical surface mass density. We take the peak positions as the cluster centers, and we measure $\gamma_t(R)$ in 5 radial bins of equal logarithmic spacing of $\Delta \log R = 0.25$ with bin centers of $R_c(i) = 0.3 \times 10^{i\Delta \log R}[h^{-1}\mathrm{Mpc}]$ where i runs from 0 to 4. We use the photo-z probability distribution functions (PDFs) of background galaxies to evaluate $\Sigma_{cr}(z_{cl}, z_s)$ following Umetsu et al. (2020, Section 3.2). The resulting $\Delta\Sigma(R)$ signals are shown in Figure 10.

We adopt the NFW model to make the model prediction of the weak lensing shear profile by a cluster. The spherical NFW density profile is specified by two parameters, the characteristic density parameter (ρ_s), and the scale radius (r_s), as $\rho_{\mathrm{NFW}}(r) = \rho_s/[r/r_s(1 + r/r_s)^2]$. We define the halo mass by the over-density mass (M_Δ) which is given by integrating the halo density profile out to the corresponding over-density radius (r_Δ) at which the mean interior density is $\Delta \times \rho_{cr}(z)$. The corresponding concentration parameter is defined by $c_\Delta = r_\Delta/r_s$. For a given set of (M_Δ, c_Δ), which is of our primary interest, the NFW parameters (ρ_s, r_s) are uniquely determined, and thus $\Delta\Sigma(R)$ is as well. Therefore we take (M_Δ, c_Δ) as fitting parameters in the likelihood analysis. We consider two cases, $\Delta = 200$ and $\Delta = 500$.

We employ the standard likelihood analysis for deriving constraints on the model parameters. The log-likelihood is

[6] For HWL16a-002, the redshift of matched XXL cluster (XLSSC 114) is taken as it is based on spectroscopic redshifts (Adami et al. 2018).

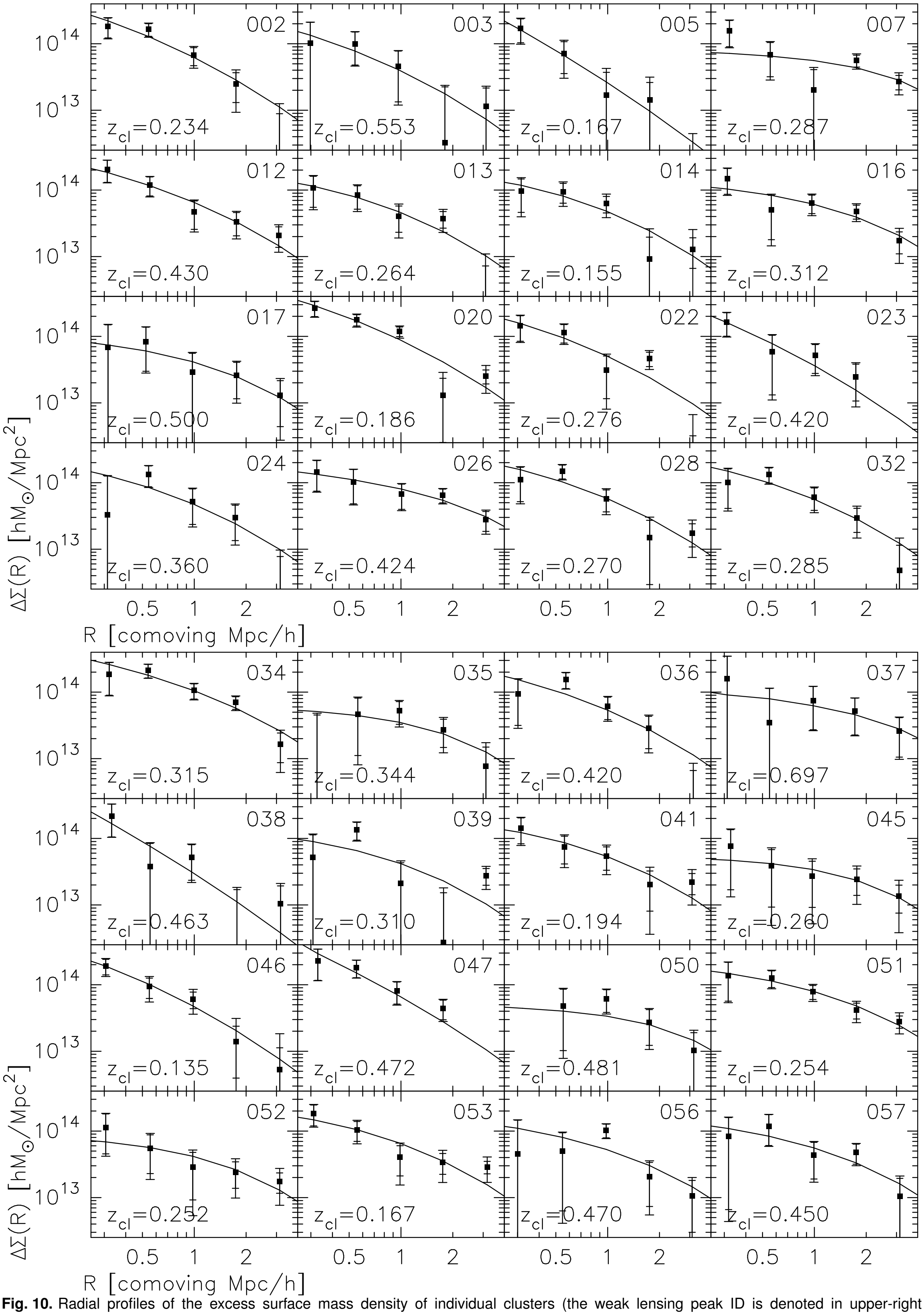

Fig. 10. Radial profiles of the excess surface mass density of individual clusters (the weak lensing peak ID is denoted in upper-right of each panel). Measurement results are plotted with filled squares with error bars; inner error bars show the shape noise components ($\sigma_{\rm shape}$) only, whereas outer error bars show the total errors being composed of shape noise, cosmic shear covariance due to large-scale structures, and intrinsic scatter components (the diagonal components of ${\rm Cov}^{\rm shape}+{\rm Cov}^{\rm lss}+{\rm Cov}^{\rm int}$, see Section 3.3 of Umetsu et al. 2020 and references therein). The best-fit NFW model in M_{200c}-c_{200c} space is shown by the solid line. Here all the results are based on the cosmological parameters inferred from the WMAP 9-year results (Hinshaw et al. 2013).

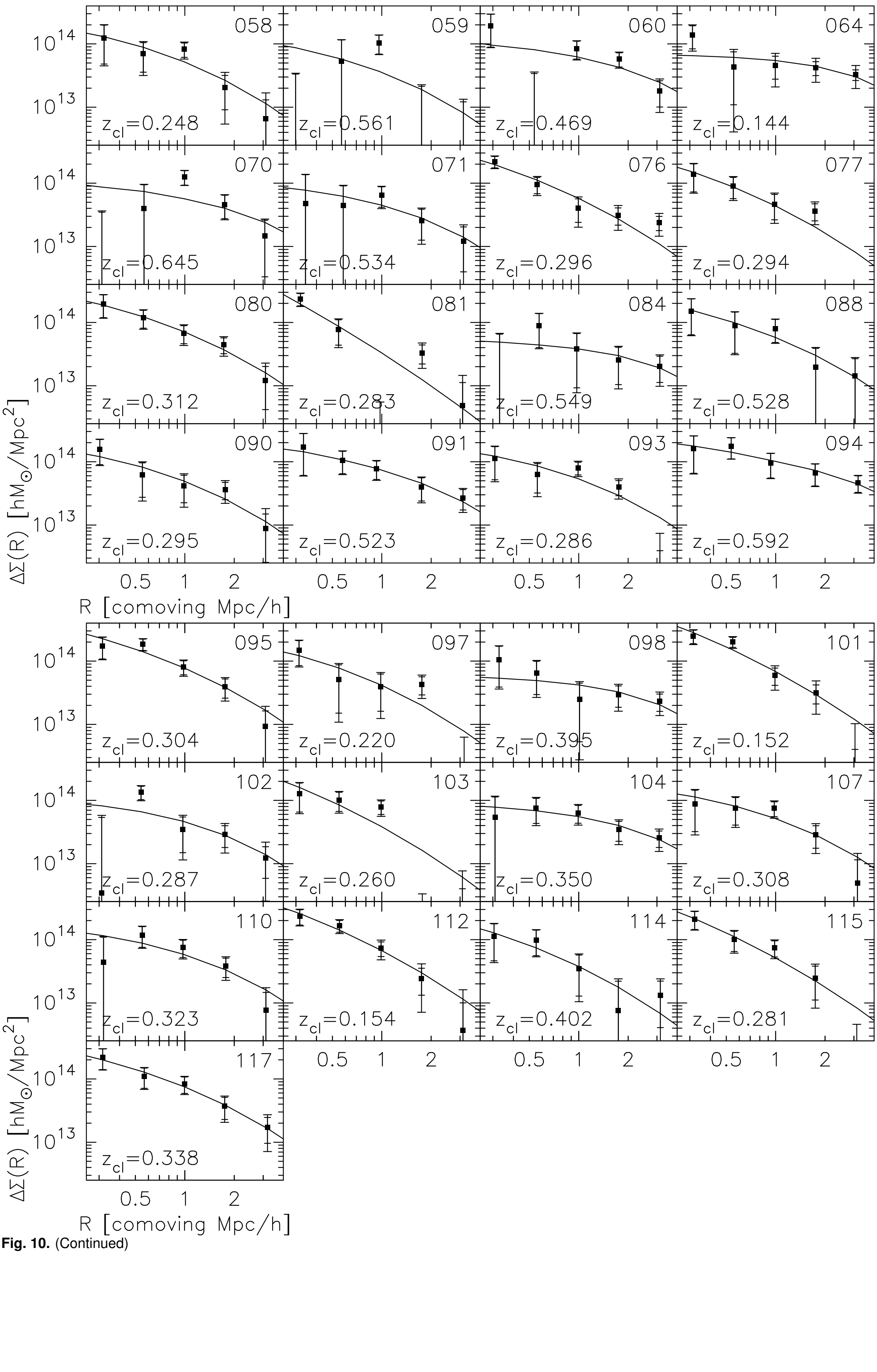

Fig. 10. (Continued)

given by,

$$-2\ln\mathcal{L}(\boldsymbol{p}) = \sum_{i,j}[d_i - m_i(\boldsymbol{p})]\mathrm{Cov}^{-1}_{ij}[d_j - m_j(\boldsymbol{p})], \quad \text{(A2)}$$

where the data vector $d_i = \Delta\Sigma(R_i)$, and $m_i(\boldsymbol{p})$ is the model prediction with the model parameters $\boldsymbol{p} = (M_\Delta, c_\Delta)$. The covariance matrix (Cov) is composed of the three components (see Umetsu et al. 2020, and references therein for detailed descriptions): The statistical uncertainty due to the galaxy shape noise ($\mathrm{Cov}^{\mathrm{shape}}$), the cosmic shear covariance due to uncorrelated large-scale structures projected along the line of sight (Hoekstra 2003) ($\mathrm{Cov}^{\mathrm{lss}}$), and the intrinsic variation of the cluster lensing signals at the fixed model parameters due to e.g., cluster asphericity, and the presence of correlated halos ($\mathrm{Cov}^{\mathrm{int}}$) (Gruen et al. 2015; Miyatake et al. 2019).

We compute the log-likelihood function over the two-parameter space in the ranges of $0.01 < M_\Delta[\times 10^{14}h^{-1}M_\odot] < 30$ and $0.01 < c_\Delta < 30$, and marginalize it to derive one-parameter posterior distributions. Peaks and 68.3% confidence intervals of marginalized posterior distributions of c_{200c}, M_{200c}, and M_{500c} are summarized in Table 5. We present two sets of results based on the cosmological parameters from the WMAP 9-year results (Hinshaw et al. 2013), and from the Planck 2018 results (Planck Collaboration et al. 2018, $\Omega_\mathrm{m} = 0.32$, $\Omega_\mathrm{b} = 0.049$, $\Omega_\Lambda = 0.68$, $n_s = 0.96$, $\sigma_8 = 0.83$, and $h = 0.67$). The differences in the derived values between two cosmological models are much smaller than the derived 68.3% confidence intervals. Note that those differences are not systematic but rather random. The reason for this is that since we take the comoving angular distance, which depends on the cosmology, for binning of $\gamma_t(R)$ measurement, the corresponding angular ranges of bins vary between two analyses and thus measured signals and errors do as well. Note that "N/A" in the results of c_{200c} means either the upper/lower bound of 68.3% confidence interval or the minimum of the marginalized likelihood function is not enclosed within the parameter range of c_{200c}. This is due to the limited coverage in R with relatively large error bars. In Figure 10, we compare the measured excess surface mass density profiles with the best-fit NFW model (based on WMAP 9-year cosmological model) in the M_{200c}-c_{200c} space, from which the reader can judge the goodness of fits.

Appendix 4 The locally normalized SN estimator

In this study, we have adopted the globally normalized SN estimator defined by equation (7) with equations (5) and (6). In some studies (for example, Hamana et al. 2015), however, the peak $SN(\boldsymbol{\theta})$ is defined by the locally normalized estimators, for which $\mathcal{K}(\boldsymbol{\theta})$ and $\sigma^2_{\mathrm{shape}}(\boldsymbol{\theta})$ are normalized by the local galaxy number density, $n_g(\boldsymbol{\theta})$, instead of the mean density $\bar{n}_g$. Here we compare those two estimators using a simple model, and using the actual weak lensing data. See Schmidt & Rozo (2011) for a related study on those estimators.

Following the same manner as introduced in Section 5.1, the local estimators are given by,

$$\mathcal{K}_L(\boldsymbol{\theta}) = \frac{1}{n_{fg} + n_{bg} + n_{cl}(\boldsymbol{\theta})}\sum_{i\in bg}\hat{\gamma}_{t,i}Q_i, \quad \text{(A3)}$$

and

$$\sigma^2_{\mathrm{shape},L}(\boldsymbol{\theta}) = \frac{1}{2[n_{fg} + n_{bg} + n_{cl}(\boldsymbol{\theta})]^2} \times\left(\sum_{i\in bg}\hat{e}_i^2Q_i^2 + \sum_{i\in fg}\hat{e}_i^2Q_i^2 + \sum_{i\in cl}\hat{e}_i^2Q_i^2\right). \quad \text{(A4)}$$

Notice that contributions from cluster member population can not be ignored at the cluster central regions where we are interested in. Thus we have,

$$SN_L(\boldsymbol{\theta}) = \frac{\sqrt{2}\sum_{bg}\hat{\gamma}_{t,i}Q_i}{\left(\sum_{bg}\hat{e}_i^2Q_i^2 + \sum_{fg}\hat{e}_i^2Q_i^2 + \sum_{cl}\hat{e}_i^2Q_i^2\right)^{1/2}}. \quad \text{(A5)}$$

Therefore, the locally defined SN is affected by the cluster member population and can be smaller than the globally defined SN [see equation (16)], though it depends on the local proportion of cluster member galaxies to background and foreground galaxies.

We examine the actual differences between the globally normalized and the locally normalized SN values using our source galaxy samples. We have generated the locally normalized SN maps for the six source samples used in this study. We evaluate locally normalized SN_L values at positions of high peaks ($SN_G \geq 5$) located in the globally normalized SN maps. This SN_G–SN_L comparison is done for six sets of SN maps. Results are shown in Figure 12, in which we find that SN_L tends to be smaller than SN_G, and that this trend is more clearly seen in lower z_{min} cases as expected. We find that SN_L is smaller than about 10 percent on average than SN_G for weak lensing maps used in this study.

We note that one may take an averaged local shape noise (that is $\langle\sigma^2_{\mathrm{shape},L}\rangle$) to define the SN, instead of the locally defined one. In this case, deriving its expression using the above manner is not straightforward, because it is necessary to take into account the covariance between numerator and denominator in equation (A4) (see Schmidt & Rozo 2011 for an approximative approach to this). Instead, we evaluate $\langle\sigma^2_{\mathrm{shape},L}\rangle$ with actual weak lensing data used

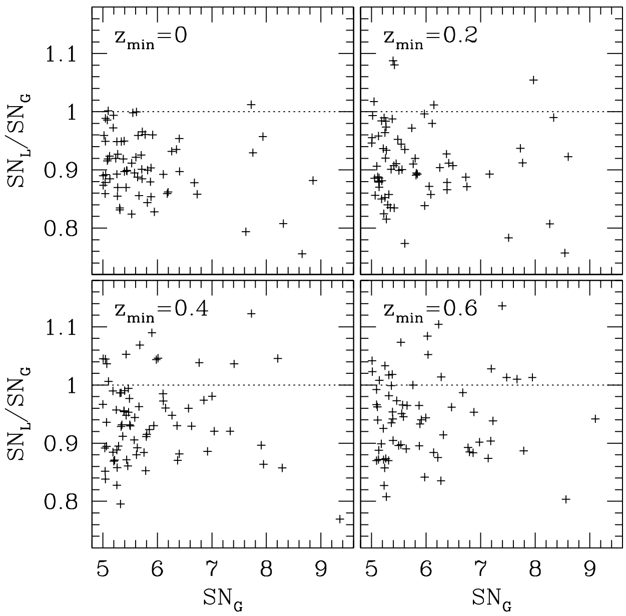

Fig. 11. Peak SN_G values in the globally normalized SN maps are compared with SN_L values at the same positions in the locally normalized SN maps. Plus marks are for high peaks ($SN_G \geq 5$) located in the globally normalized SN maps. Different panels are for different source samples with $z_{\rm min}$ being shown in each panel.

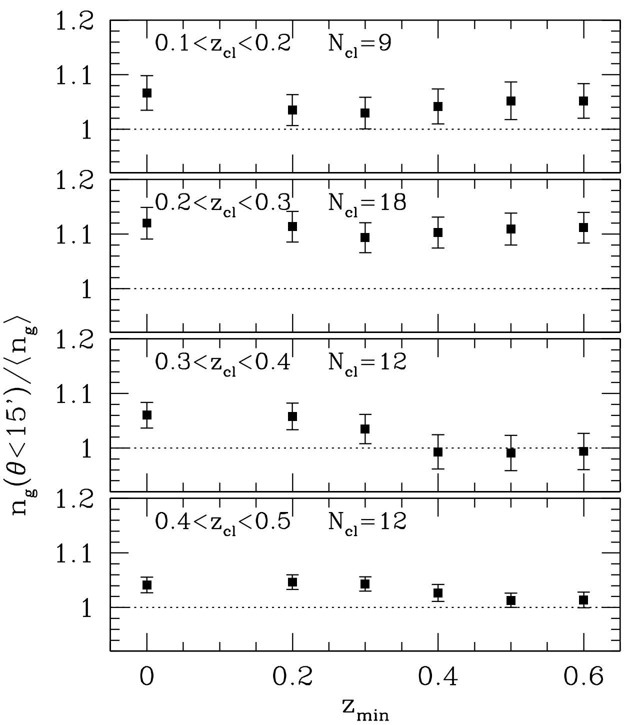

Fig. 12. Shown is the local galaxy number density at cluster regions, which is defined by the mean number density within an angular radius of 15 arcmin from peak positions, normalized by the global mean galaxy number density. Weak lensing secure clusters are used, and are divided into four sub-samples based on the cluster redshifts (denoted in panels). The horizontal axis is $z_{\rm min}$ of source galaxy samples. For each sub-sample and each source galaxy sample, the mean and its 1-σ error among the clusters (the number of clusters in each sub-sample is given in each panel) are plotted.

in this study and compare it with $\langle\sigma^2_{{\rm shape},G}\rangle$. We find that the two are very close; $\langle\sigma^2_{{\rm shape},L}\rangle^{1/2}$ is only slightly smaller than $\langle\sigma^2_{{\rm shape},G}\rangle^{1/2}$ (to be specific, the fractional difference is smaller than 0.5 percent). Therefore, replacing $\sigma^2_{{\rm shape},L}(\boldsymbol{\theta})$ with $\langle\sigma^2_{{\rm shape},L}\rangle$ does not mitigate the dilution effect, but an additional $n_{cl}(\boldsymbol{\theta})$ term in the normalization of $\mathcal{K}_L(\boldsymbol{\theta})$ suppresses the peak signal [compare equations (13) with (A3)]. We measure n_{cl} from our data; in doing this, we have defined the local galaxy number density at cluster regions by the mean number density within a circular area with an angular radius of 15 arcmin from peak positions.[7] Results are shown in Figure 12 for four cluster redshift ranges and six source samples, in which we find that for $z_{\rm min}$ from 0 to 0.3, the galaxy density excess is 5-10 percent; while for higher $z_{\rm min}$, it is consistent with zero for higher redshift clusters ($0.3 < z_{cl} < 0.5$), but the excess is still 5-10 percent for lower redshift clusters. It follows from these results that for low-$z_{\rm min}$ source samples, a peak SN from the globally normalized estimator can be 5-10 percent larger than one from the locally normalized estimator.

We note that the decreasing trend of the number excess at higher $z_{\rm min}$ seen in higher redshift clusters is expected, as $z_{\rm min}$-cut may exclude cluster member galaxies of clusters at $z_{cl} < z_{\rm min}$. However, the trend is not seen in the lower redshift clusters. The reason for this is not understood well; possible causes are the line-of-sight projection of undiscovered clusters at higher redshifts, and errors in photo-z (cluster member galaxies at a low-z are mis-estimated as higher-z galaxies). We are not going into this issue in this study but leave it for a future study.

[7] We note that the *local galaxy number density* is not uniquely defined, because it is necessary to define a *local scale*, or an *averaging scheme*. Thus the estimated values given there are not general but are specific to our definition of the local galaxy number density.

Table 3. Summary of weak lensing merged peaks. First column is the merged peak ID, the second to fifth columns are for information of weak lensing peaks (see Section 3.3), the sixth to ninth columns are for information of matched CAMIRA-HSC clusters (see Section 4), and the last columns is for matched known clusters in Adami et al. (2018) (XXL clusters, see Appendix 1.2), Abell et al. (1989) (Abell clusters), and Miyazaki et al. (2018a, cited by M18 in this table) (weak lensing peaks, see Appendix 1.3).

Weak lensing					CAMIRA-HSC				Note
ID	$SN_{\rm max}$	$z_{\rm opt}$	RA	Dec	ID	z_{cl}	$N_{\rm mem}$	$\theta_{\rm sep}$	
			J2000.0 [°]					[′]	
HWL16a-001	5.19	0.0	30.3800	−5.5078	-	-	-	-	M18 rank 29
HWL16a-002	7.23	0.6	30.4273	−5.0219	31	0.809	21.4	1.7	XLSSC 114 ($z = 0.234$)
									M18 rank 13
HWL16a-003	5.22	0.5	31.2073	−3.0587	65	0.553	29.2	1.3	
HWL16a-004	5.87	0.6	31.3577	−5.7178	74	0.290	43.5	0.9	XLSSC 106 ($z = 0.300$)
					71	0.697	24.1	3.8	
HWL16a-005	5.24	0.5	31.4584	−3.3714	76	0.167	21.6	1.3	
HWL16a-006	5.46	0.3	32.0082	−3.4128	94	0.204	15.7	2.7	
HWL16a-007	6.53	0.3	33.1112	−5.6214	149	0.287	64.0	1.7	XLSSC 111 ($z = 0.300$)
HWL16a-008	5.46	0.3	33.1188	−5.5365	149	0.287	64.0	4.0	XLSSC 117 ($z = 0.298$)
									M18 rank 58
HWL16a-009	6.11	0.0	33.3625	−2.9126	165	0.150	40.4	2.4	M18 rank 16
HWL16a-010	5.97	0.2	33.4777	−2.8852	174	0.274	16.1	2.8	M18 rank 63
					176	1.018	29.6	4.2	
HWL16a-011	5.12	0.6	33.8206	−2.7029	-	-	-	-	
HWL16a-012	6.77	0.6	35.4434	−3.7668	252	0.430	68.3	0.3	XLSSC 006 ($z = 0.429$)
HWL16a-013	5.31	0.6	36.1229	−4.2378	285	0.264	15.1	0.9	XLSSC 044 ($z = 0.263$)
HWL16a-014	6.38	0.2	36.3758	−4.2496	293	0.155	18.1	0.7	XLSSC 041 ($z = 0.142$)
									M18 rank 36
HWL16a-015	6.04	0.6	37.0512	−5.5929	-	-	-	-	
HWL16a-016	7.95	0.4	37.3963	−3.6121	324	0.312	57.1	0.4	M18 rank 9
HWL16a-017	5.45	0.3	37.5572	−5.6526	327	0.500	22.3	1.8	XLSSC 169 ($z = 0.498$)
HWL16a-018	5.26	0.2	37.7796	−5.5840	-	-	-	-	
HWL16a-019	5.08	0.0	37.8096	−4.4738	338	1.011	16.3	5.0	
HWL16a-020	9.68	0.3	37.9163	−4.8799	343	0.187	116.8	0.4	XLSSC 091 ($z = 0.186$)
									Abell 362 ($z = 0.184$)
									M18 rank 2
HWL16a-021	6.06	0.2	38.1182	−4.7890	355	0.276	33.1	3.5	XLSSC 151 ($z = 0.189$)
									XLSSC 152 ($z = 0.205$)
									M18 rank 28
HWL16a-022	6.59	0.3	38.1580	−4.7513	355	0.276	33.1	0.4	XLSSC 151 ($z = 0.189$)
HWL16a-023	5.30	0.3	38.3915	−5.5027	362	0.420	46.9	0.4	XLSSC 105 ($z = 0.432$)
HWL16a-024	5.11	0.5	129.3206	1.6069	401	0.360	36.5	0.8	
HWL16a-025	5.64	0.0	130.3706	0.4379	433	0.413	19.0	0.4	M18 rank 22
					430	0.454	24.4	4.0	
					435	0.215	21.3	4.1	
HWL16a-026	7.93	0.5	130.5895	1.6473	438	0.424	78.9	0.4	
HWL16a-027	5.11	0.4	131.0585	1.0644	449	0.323	29.1	1.5	
					448	0.661	16.8	1.8	
HWL16a-028	6.98	0.6	133.1296	0.4041	505	0.270	43.2	1.6	M18 rank 18
HWL16a-029	5.27	0.6	135.9841	1.4088	591	0.817	16.1	2.0	
					592	0.665	15.6	2.8	
HWL16a-030	5.16	0.3	136.0810	0.5865	594	0.399	16.1	2.7	
					593	0.303	26.8	4.9	

Table 3. (Continued)

Weak lensing					CAMIRA-HSC				Note
ID	$SN_{\max}$	$z_{\rm opt}$	RA	Dec	ID	z_{cl}	$N_{\rm mem}$	$\theta_{\rm sep}$	
			J2000.0 [°]					[′]	
HWL16a-031	5.18	0.2	136.8921	−0.0580	628	1.062	21.4	0.4	
HWL16a-032	8.31	0.0	138.4612	−0.7631	686	0.285	36.1	1.0	M18 rank 4
HWL16a-033	5.55	0.0	138.5051	1.6655	691	0.380	15.6	4.6	M18 rank 20
HWL16a-034	7.72	0.4	139.0387	−0.3966	716	0.315	78.5	1.4	Abell 776 ($z = 0.336$)
									M18 rank 8
HWL16a-035	5.29	0.4	139.3198	0.9985	733	0.344	24.7	1.5	
HWL16a-036	5.99	0.6	139.3405	3.8281	734	0.420	22.9	0.4	
HWL16a-037	5.18	0.6	140.0954	1.5748	770	0.697	55.0	0.3	
HWL16a-038	5.03	0.3	140.1431	0.7907	771	0.463	25.2	1.3	
HWL16a-039	5.88	0.0	140.4154	−0.2491	784	0.310	29.1	1.7	M18 rank 39
HWL16a-040	5.97	0.6	140.5592	−0.1323	793	0.794	17.5	0.9	
HWL16a-041	6.01	0.3	140.6790	2.1327	798	0.194	24.8	0.2	M18 rank 30
HWL16a-042	5.53	0.0	177.1051	−0.6610	864	0.419	25.9	3.5	M18 rank 19
					861	0.898	15.9	4.3	
HWL16a-043	5.49	0.6	177.1322	0.0088	860	1.080	27.6	5.0	
HWL16a-044	6.14	0.6	177.2646	0.2836	870	0.260	16.5	4.1	
HWL16a-045	5.26	0.4	177.2946	0.3636	870	0.260	16.5	1.1	
HWL16a-046	8.07	0.5	177.5842	−0.6009	878	0.135	51.8	0.6	Abell 1392 ($z = 0.139$)
									M18 rank 10
HWL16a-047	7.05	0.4	178.0615	0.5187	892	0.472	61.0	0.3	M18 rank 17
HWL16a-048	6.11	0.4	178.0989	−0.5111	893	0.311	15.7	2.2	M18 rank 32
HWL16a-049	5.22	0.4	178.6288	−0.1237	909	0.246	30.6	3.4	
					916	0.548	19.0	3.6	
					912	0.892	17.7	5.0	
HWL16a-050	5.05	0.4	178.8288	0.8712	922	0.481	21.9	1.1	
HWL16a-051	7.75	0.0	179.0517	−0.3490	928	0.254	66.9	1.5	M18 rank 5
HWL16a-052	5.25	0.4	179.6138	−0.0412	942	0.252	29.5	1.7	
HWL16a-053	6.36	0.3	180.4286	−0.1839	966	0.167	45.8	1.2	Abell 1445 ($z = 0.169$)
									M18 rank 12
HWL16a-054	5.01	0.6	180.4536	−0.4986	968	0.322	24.5	0.7	
					967	0.162	24.0	0.9	
HWL16a-055	5.39	0.4	180.6834	0.9709	978	0.568	33.7	0.7	
					982	0.434	23.2	3.3	
HWL16a-056	6.88	0.6	181.3878	−0.6432	994	0.470	40.7	0.7	
HWL16a-057	5.32	0.4	210.7874	−0.3084	1037	0.450	35.1	0.0	
HWL16a-058	5.25	0.6	211.2955	−0.1472	1046	0.248	27.5	0.7	
HWL16a-059	5.52	0.5	211.7872	−0.2717	1057	0.561	48.3	1.3	
HWL16a-060	7.33	0.4	211.9925	−0.4857	1062	0.469	34.0	0.9	M18 rank 35
HWL16a-061	5.26	0.4	212.3195	−0.1997	-	-	-	-	
HWL16a-062	5.42	0.2	213.6054	−0.3669	1103	0.144	60.0	1.1	M18 rank 54
					1105	1.024	15.4	3.6	
HWL16a-063	5.07	0.4	213.7248	−0.3423	1105	1.024	15.4	4.4	
HWL16a-064	5.44	0.0	213.7770	−0.4892	1112	0.144	38.8	0.5	Abell 1882 ($z = 0.137$)
									M18 rank 26
HWL16a-065	7.16	0.2	213.8891	−0.0527	-	-	-	-	M18 rank 23
HWL16a-066	5.63	0.5	214.6762	−0.0506	-	-	-	-	
HWL16a-067	5.13	0.0	214.8009	0.2418	-	-	-	-	

Table 3. (Continued)

Weak lensing					CAMIRA-HSC				Note
ID	$SN_{\rm max}$	$z_{\rm opt}$	RA	Dec	ID	z_{cl}	$N_{\rm mem}$	$\theta_{\rm sep}$	
			J2000.0 [°]					[′]	
HWL16a-068	5.31	0.0	215.0330	0.9984	1155	0.322	16.6	2.8	
					1157	0.515	46.3	3.9	
HWL16a-069	7.18	0.6	215.0729	0.9557	1157	0.515	46.3	0.5	M18 rank 33
					1155	0.322	16.6	1.2	
					1161	0.168	15.3	4.7	
HWL16a-070	6.22	0.6	215.2574	0.3665	1164	0.645	47.6	1.4	
HWL16a-071	5.38	0.5	215.9165	0.4491	1191	0.534	29.4	0.5	
HWL16a-072	5.11	0.6	216.0089	0.1418	1195	0.539	39.1	0.8	
					1192	0.319	17.8	2.9	
HWL16a-073	7.02	0.5	216.6510	0.8016	1220	0.604	18.8	3.8	M18 rank 62
HWL16a-074	5.01	0.0	216.6535	−0.0903	-	-	-	-	
HWL16a-075	5.65	0.3	216.6760	0.1643	1222	0.531	25.3	2.2	
HWL16a-076	9.36	0.5	216.7785	0.7267	1226	0.296	24.2	0.4	M18 rank 14
HWL16a-077	5.46	0.6	216.8310	0.9541	1231	0.294	36.6	2.0	
HWL16a-078	5.28	0.0	216.8484	−0.2403	1229	0.164	19.3	4.2	
HWL16a-079	5.05	0.0	216.8659	−0.1978	-	-	-	-	M18 rank 40
HWL16a-080	6.14	0.5	217.6808	0.8093	1244	0.312	35.4	0.6	M18 rank 47
HWL16a-081	5.66	0.4	218.8457	−0.3931	1273	0.283	27.3	1.3	
HWL16a-082	5.49	0.4	218.8858	−1.1228	1274	0.756	15.6	3.5	
					1277	0.260	24.4	4.1	
HWL16a-083	5.82	0.0	219.2131	−0.7026	1288	0.198	18.4	4.1	M18 rank 25
HWL16a-084	5.42	0.3	220.0846	−0.6101	1322	0.549	39.6	1.4	
HWL16a-085	5.82	0.0	220.4015	−0.9068	1339	0.536	52.9	1.0	M18 rank 53
					1341	0.884	17.3	2.5	
HWL16a-086	5.23	0.5	220.4589	−0.8247	1344	0.149	29.3	1.6	
					1341	0.884	17.3	4.9	
HWL16a-087	5.02	0.0	220.5909	0.3367	1347	0.166	21.0	2.6	M18 rank 64
HWL16a-088	6.01	0.4	220.7952	1.0452	1351	0.528	40.2	0.6	M18 rank 48
HWL16a-089	5.71	0.0	221.0371	0.1743	-	-	-	-	M18 rank 11
HWL16a-090	5.39	0.6	221.1442	0.2464	1363	0.295	54.2	1.4	
HWL16a-091	5.91	0.6	221.1917	−0.6694	1366	0.523	36.6	0.4	
HWL16a-092	5.05	0.3	221.2090	0.2015	-	-	-	-	
HWL16a-093	6.80	0.6	221.3335	0.1116	1371	0.286	32.7	0.2	M18 rank 57
HWL16a-094	6.49	0.2	223.0801	0.1689	1417	0.592	26.1	0.3	M18 rank 34
HWL16a-095	7.66	0.6	223.0929	−0.9713	1418	0.304	38.4	0.2	M18 rank 42
HWL16a-096	5.02	0.2	223.9242	−0.3384	-	-	-	-	
HWL16a-097	5.05	0.0	224.2746	0.1164	1443	0.220	25.9	0.6	
HWL16a-098	5.58	0.4	224.6567	0.4858	1454	0.395	18.1	0.4	
HWL16a-099	5.76	0.2	244.4326	42.5427	1530	0.285	30.8	1.2	
					1528	0.598	17.9	4.1	
HWL16a-100	5.78	0.0	245.0550	42.5052	1540	0.141	27.4	0.9	M18 rank 24
					1543	0.800	22.7	4.9	
HWL16a-101	8.24	0.3	245.3758	42.7648	1547	0.152	33.7	0.6	Abell 2183 ($z = 0.136$) M18 rank 1
HWL16a-102	5.04	0.4	246.1339	43.3203	1557	0.287	26.1	0.8	
HWL16a-103	5.58	0.0	246.5173	43.7147	1561	0.260	17.1	1.1	
HWL16a-104	6.31	0.6	333.0522	−0.1334	1622	0.350	30.9	0.4	M18 rank 44

Table 3. (Continued)

Weak lensing					CAMIRA-HSC				Note
ID	$SN_{\rm max}$	$z_{\rm opt}$	RA	Dec	ID	z_{cl}	$N_{\rm mem}$	$\theta_{\rm sep}$	
			J2000.0 [°]					[′]	
HWL16a-105	5.36	0.3	333.3515	−0.2017	1628	0.100	19.7	3.8	
					1630	0.357	33.3	4.3	
HWL16a-106	5.55	0.3	333.3714	−0.1542	1628	0.100	19.7	1.4	M18 rank 50
					1630	0.357	33.3	3.9	
HWL16a-107	5.57	0.6	333.5929	0.7956	1635	0.308	26.7	0.6	
HWL16a-108	5.14	0.2	333.6801	1.1171	1637	0.469	25.2	2.2	
					1638	0.759	18.5	4.3	
HWL16a-109	5.32	0.5	333.7900	1.0422	1639	0.702	26.7	1.2	
HWL16a-110	5.91	0.3	335.2140	0.9704	1664	0.323	22.1	0.1	
HWL16a-111	5.43	0.4	335.4040	1.3854	1670	0.790	22.8	2.4	M18 rank 56
					1669	0.324	16.9	3.3	
HWL16a-112	8.34	0.2	336.0366	0.3331	1683	0.154	44.3	0.5	M18 rank 3
HWL16a-113	6.75	0.2	336.2291	−0.3668	1688	0.308	33.1	0.8	M18 rank 21
					1687	0.140	19.5	1.0	
HWL16a-114	5.63	0.4	336.4066	−0.3068	1694	0.402	17.8	0.2	
HWL16a-115	6.58	0.5	336.4217	1.0730	1696	0.281	49.9	0.8	M18 rank 52
HWL16a-116	5.31	0.0	336.9540	0.1141	1707	0.410	17.3	2.0	
HWL16a-117	6.23	0.6	337.1293	1.7135	1709	0.338	31.5	0.6	M18 rank 61
HWL16a-118	5.66	0.5	338.0182	0.0231	-	-	-	-	M18 rank 59
HWL16a-119	5.39	0.6	338.0183	0.2288	1724	1.013	18.6	3.2	
HWL16a-120	5.13	0.6	338.5233	1.6997	1733	0.246	16.0	3.8	
HWL16a-121	5.39	0.2	338.9150	1.4837	-	-	-	-	Abell 2457 ($z = 0.059$)
									M18 rank 6
HWL16a-122	6.47	0.6	339.1320	1.5266	-	-	-	-	
HWL16a-123	5.54	0.6	339.3176	−0.3629	-	-	-	-	
HWL16a-124	5.65	0.0	339.7643	0.6652	1748	0.264	19.4	1.2	M18 rank 65
					1749	0.200	19.6	3.5	

Table 4. Summary of known cluster counterparts of 17 weak lensing merged peaks which have no CAMIRA-HSC cluster within 5 arcmin radius from the peak positions. A known cluster database taken from a compilation by `NASA/IPAC Extragalactic Database` (NED) was used for this counterpart search.

ID	Cluster name	z_{cl}	${\theta_{\rm sep}}^a$ [arcmin]	Ref
HWL16a-001	-	-	-	-
HWL16a-011	-	-	-	-
HWL16a-015	CFHTLS W1-2593	0.30	1.4	Durret et al. (2011)
	CFHTLS W1-2588	0.68	4.1	Durret et al. (2011)
	CFHT-W CL J022757.5−053537	0.32	4.9	Wen & Han (2011)
HWL16a-018	CFHT-W CL J023111.0−0536	0.67	1.9	Wen & Han (2011)
	CFHTLS W1-2864	0.60	2.8	Durret et al. (2011)
	CFHTLS W1-2588	0.68	2.9	Durret et al. (2011)
	CFHTLS W1-2589	1.00	3.2	Durret et al. (2011)
HWL16a-061	-	-	-	-
HWL16a-065	SDSS CE J213.904556−00.069648	0.29	1.4	Goto et al. (2002)
	WHL J141527.6−000319	0.15	1.5	Wen et al. (2009)
	SDSS CE J213.843536−00.001681	0.29	4.1	Goto et al. (2002)
	SDSS CE J213.919922+00.023597	0.33	4.9	Goto et al. (2002)
HWL16a-066	SDSS CE J214.633743−00.016635	0.23	3.3	Goto et al. (2002)
HWL16a-067	SDSS CE J214.788757+00.220532	0.44	1.5	Goto et al. (2002)
HWL16a-074	GMBCG J216.67104−00.08426	0.39	1.1	Hao et al. (2010)
	SDSS CE J216.649841−00.110289	0.27	1.2	Goto et al. (2002)
	GMBCG J216.63912−00.10900	0.25	1.4	Hao et al. (2010)
	SDSS CE J216.635178−00.044207	0.42	3.0	Goto et al. (2002)
	GMBCG J216.67010−00.03407	0.40	3.5	Hao et al. (2010)
HWL16a-079	SDSS CE J16.867157−00.209108	0.18	0.7	Goto et al. (2002)
	SDSS CE J216.868240−00.171960	0.35	1.6	Goto et al. (2002)
	SDSS CE J216.852905−00.249845	0.18	3.2	Goto et al. (2002)
HWL16a-089	SDSS CE J221.044815+00.172764	0.30	0.2	Goto et al. (2002)
	GMBCG J221.00862+00.12188	0.29	3.6	Hao et al. (2010)
HWL16a-092	FAC2011 CL 0061	0.62	1.2	Farrens et al. (2011)
	GMBCG J221.15835+00.19581	0.43	3.1	Hao et al. (2010)
	WHL J144437.5+001402	0.31	3.7	Wen et al. (2009)
	SDSS CE J221.230865+00.138749	0.27	4.0	Goto et al. (2002)
	MaxBCG J221.20075+00.12862	0.29	4.4	Koester et al. (2007)
	SDSS CE J221.138031+00.233130	0.30	4.7	Goto et al. (2002)
HWL16a-096	-	-	-	-
HWL16a-118	-	-	-	-
HWL16a-121	WHL J223540.8+012906	0.058	0.3	Wen et al. (2009)
	MCXC J2235.6+0128	0.060	0.8	Piffaretti et al. (2011)
	ABELL 2457	0.059	1.5	Abell et al. (1989)
HWL16a-122	-	-	-	-
HWL16a-123	-	-	-	-

[a] The angular separation between the weak lensing peak position and the cluster position.

Table 5. Results of the likelihood analysis of the surface mass density profile of individual clusters based on NFW model (see Appendix 3). Cluster redshifts (z_{cl}) are taken from the estimated redshift of matched CAMIRA clusters except for HWL16a-002 for which the redshift of matched XXL cluster (XLSSC 114) is taken (marked by *). Peaks and 68.3% confidence intervals of marginalized posterior distributions of c_{200c}, M_{200c}, M_{500c} are summarized. The results based on the cosmological parameters from the WMAP 9-year (Hinshaw et al. 2013, $\Omega_{\rm m}=0.279$, $\Omega_{\rm b}=0.046$, $\Omega_\Lambda=0.721$, $n_s=0.97$, $\sigma_8=0.82$, and $h=0.7$), and Planck 2018 results (Planck Collaboration et al. 2018, $\Omega_{\rm m}=0.32$, $\Omega_{\rm b}=0.049$, $\Omega_\Lambda=0.68$, $n_s=0.96$, $\sigma_8=0.83$, and $h=0.67$) are presented. "N/A" in the results of c_{200c} means either the upper/lower bound of 68.3% confidence interval or the minimum of the marginalized log-likelihood function is not enclosed within the parameter range of $0.01 \le c_\Delta \le 30$.

		WMAP9 cosmology			Planck2018 cosmology		
ID	z_{cl}	c_{200c}	M_{200c} $[10^{14}h^{-1}M_\odot]$	M_{500c} $[10^{14}h^{-1}M_\odot]$	c_{200c}	M_{200c} $[10^{14}h^{-1}M_\odot]$	M_{500c} $[10^{14}h^{-1}M_\odot]$
HWL16a-002	0.234^*	$5.34^{+5.19}_{-2.23}$	$1.91^{+0.74}_{-0.48}$	$1.51^{+0.49}_{-0.36}$	$4.74^{+4.74}_{-2.03}$	$1.85^{+0.77}_{-0.49}$	$1.46^{+0.50}_{-0.37}$
HWL16a-003	0.553	$2.45^{+5.94}_{-1.85}$	$1.10^{+0.69}_{-0.54}$	$0.86^{+0.49}_{-0.42}$	$2.76^{+7.11}_{-2.00}$	$1.08^{+0.66}_{-0.53}$	$0.85^{+0.47}_{-0.41}$
HWL16a-005	0.167	$9.89^{+\rm N/A}_{-7.45}$	$0.89^{+0.41}_{-0.36}$	$0.72^{+0.32}_{-0.29}$	$8.64^{+\rm N/A}_{-6.48}$	$0.90^{+0.43}_{-0.37}$	$0.73^{+0.33}_{-0.30}$
HWL16a-007	0.287	$0.50^{+0.70}_{-0.43}$	$3.99^{+1.96}_{-1.66}$	$1.78^{+0.81}_{-0.75}$	$0.43^{+0.68}_{-0.41}$	$3.89^{+2.16}_{-2.12}$	$1.55^{+0.96}_{-0.68}$
HWL16a-012	0.430	$3.01^{+3.22}_{-1.54}$	$2.03^{+1.19}_{-0.57}$	$1.60^{+0.66}_{-0.43}$	$2.29^{+2.74}_{-1.30}$	$1.89^{+1.25}_{-0.56}$	$1.49^{+0.66}_{-0.42}$
HWL16a-013	0.264	$2.14^{+2.43}_{-1.15}$	$1.11^{+0.75}_{-0.39}$	$0.86^{+0.41}_{-0.29}$	$2.46^{+3.11}_{-1.34}$	$1.15^{+0.62}_{-0.39}$	$0.90^{+0.38}_{-0.29}$
HWL16a-014	0.155	$2.07^{+2.41}_{-1.15}$	$1.05^{+0.69}_{-0.40}$	$0.81^{+0.40}_{-0.29}$	$2.02^{+2.46}_{-1.15}$	$1.05^{+0.67}_{-0.39}$	$0.82^{+0.40}_{-0.30}$
HWL16a-016	0.312	$1.20^{+1.03}_{-0.63}$	$3.22^{+1.56}_{-1.39}$	$1.77^{+0.72}_{-0.69}$	$1.19^{+1.09}_{-0.64}$	$3.15^{+1.73}_{-1.72}$	$1.70^{+0.81}_{-0.71}$
HWL16a-017	0.500	$0.98^{+2.09}_{-0.88}$	$1.00^{+0.81}_{-0.51}$	$0.76^{+0.48}_{-0.38}$	$0.75^{+1.84}_{-\rm N/A}$	$0.93^{+0.79}_{-0.50}$	$0.70^{+0.48}_{-0.37}$
HWL16a-020	0.186	$5.39^{+3.74}_{-1.95}$	$3.06^{+1.29}_{-0.76}$	$2.41^{+0.79}_{-0.55}$	$5.14^{+3.64}_{-1.87}$	$3.06^{+1.39}_{-0.79}$	$2.40^{+0.85}_{-0.57}$
HWL16a-022	0.276	$3.42^{+4.07}_{-1.71}$	$1.38^{+0.66}_{-0.42}$	$1.09^{+0.41}_{-0.33}$	$3.06^{+3.62}_{-1.55}$	$1.35^{+0.69}_{-0.44}$	$1.05^{+0.44}_{-0.32}$
HWL16a-023	0.420	$5.19^{+13.79}_{-3.00}$	$1.12^{+0.50}_{-0.40}$	$0.89^{+0.36}_{-0.31}$	$5.10^{+14.04}_{-2.97}$	$1.13^{+0.50}_{-0.40}$	$0.90^{+0.36}_{-0.32}$
HWL16a-024	0.360	$2.57^{+3.43}_{-1.48}$	$1.29^{+0.79}_{-0.55}$	$0.99^{+0.51}_{-0.41}$	$2.24^{+3.00}_{-1.34}$	$1.28^{+0.83}_{-0.56}$	$0.98^{+0.52}_{-0.42}$
HWL16a-026	0.424	$1.20^{+0.89}_{-0.63}$	$6.20^{+2.60}_{-2.07}$	$3.34^{+1.10}_{-0.98}$	$1.21^{+0.90}_{-0.63}$	$6.04^{+2.63}_{-2.09}$	$3.27^{+1.12}_{-1.00}$
HWL16a-028	0.270	$2.93^{+2.59}_{-1.36}$	$1.63^{+1.13}_{-0.54}$	$1.25^{+0.60}_{-0.39}$	$2.95^{+2.66}_{-1.37}$	$1.64^{+1.13}_{-0.53}$	$1.27^{+0.60}_{-0.39}$
HWL16a-032	0.285	$2.87^{+2.40}_{-1.27}$	$1.61^{+1.15}_{-0.55}$	$1.22^{+0.60}_{-0.39}$	$2.83^{+2.52}_{-1.29}$	$1.55^{+1.11}_{-0.52}$	$1.19^{+0.59}_{-0.37}$
HWL16a-034	0.315	$3.22^{+1.67}_{-1.08}$	$5.69^{+1.87}_{-1.62}$	$3.94^{+1.03}_{-0.95}$	$3.10^{+1.66}_{-1.06}$	$5.61^{+1.96}_{-1.68}$	$3.87^{+1.07}_{-0.99}$
HWL16a-035	0.344	$0.73^{+1.02}_{-0.55}$	$0.80^{+1.24}_{-0.49}$	$0.54^{+0.46}_{-0.32}$	$0.67^{+0.96}_{-0.53}$	$0.74^{+1.33}_{-0.48}$	$0.50^{+0.48}_{-0.31}$
HWL16a-036	0.420	$3.09^{+2.55}_{-1.36}$	$1.55^{+1.15}_{-0.56}$	$1.17^{+0.64}_{-0.40}$	$2.97^{+2.49}_{-1.32}$	$1.51^{+1.17}_{-0.56}$	$1.15^{+0.64}_{-0.40}$
HWL16a-037	0.697	$0.32^{+1.35}_{-\rm N/A}$	$2.08^{+2.58}_{-1.10}$	$1.57^{+1.22}_{-0.82}$	$0.40^{+1.39}_{-\rm N/A}$	$1.97^{+2.09}_{-1.06}$	$1.49^{+1.11}_{-0.80}$
HWL16a-038	0.463	$3.25^{+\rm N/A}_{-2.68}$	$1.10^{+0.62}_{-0.53}$	$0.89^{+0.46}_{-0.42}$	$3.33^{+\rm N/A}_{-2.79}$	$1.06^{+0.61}_{-0.53}$	$0.86^{+0.46}_{-0.42}$
HWL16a-039	0.310	$0.95^{+2.51}_{-\rm N/A}$	$0.90^{+0.70}_{-0.41}$	$0.69^{+0.40}_{-0.31}$	$1.52^{+3.43}_{-\rm N/A}$	$0.98^{+0.59}_{-0.40}$	$0.77^{+0.38}_{-0.32}$
HWL16a-041	0.194	$1.69^{+2.47}_{-1.11}$	$1.24^{+0.74}_{-0.44}$	$0.97^{+0.44}_{-0.33}$	$1.74^{+2.82}_{-1.20}$	$1.19^{+0.65}_{-0.43}$	$0.93^{+0.42}_{-0.32}$
HWL16a-045	0.260	$0.55^{+1.30}_{-0.52}$	$0.70^{+0.51}_{-0.35}$	$0.54^{+0.32}_{-0.27}$	$0.52^{+1.32}_{-\rm N/A}$	$0.68^{+0.49}_{-0.34}$	$0.53^{+0.32}_{-0.27}$
HWL16a-046	0.135	$4.88^{+8.25}_{-2.49}$	$1.31^{+0.50}_{-0.37}$	$1.05^{+0.34}_{-0.29}$	$4.41^{+7.59}_{-2.30}$	$1.29^{+0.52}_{-0.37}$	$1.03^{+0.36}_{-0.29}$
HWL16a-047	0.472	$9.26^{+\rm N/A}_{-4.79}$	$2.50^{+0.74}_{-0.63}$	$2.01^{+0.55}_{-0.49}$	$10.26^{+\rm N/A}_{-5.51}$	$2.53^{+0.73}_{-0.63}$	$2.04^{+0.55}_{-0.50}$
HWL16a-050	0.481	$0.50^{+0.79}_{-0.46}$	$1.30^{+1.60}_{-1.13}$	$0.46^{+0.67}_{-0.35}$	$0.44^{+0.73}_{-\rm N/A}$	$1.53^{+1.63}_{-1.35}$	$0.48^{+0.71}_{-0.37}$
HWL16a-051	0.254	$1.67^{+1.23}_{-0.78}$	$4.40^{+1.73}_{-1.43}$	$2.66^{+0.80}_{-0.73}$	$1.43^{+1.16}_{-0.72}$	$4.28^{+1.89}_{-1.54}$	$2.50^{+0.85}_{-0.77}$
HWL16a-052	0.252	$0.76^{+1.83}_{-0.68}$	$0.92^{+0.60}_{-0.39}$	$0.71^{+0.37}_{-0.29}$	$0.67^{+1.63}_{-0.63}$	$0.89^{+0.59}_{-0.40}$	$0.69^{+0.37}_{-0.30}$
HWL16a-053	0.167	$1.66^{+2.45}_{-1.12}$	$1.59^{+1.07}_{-0.49}$	$1.25^{+0.58}_{-0.37}$	$1.68^{+2.72}_{-1.18}$	$1.53^{+0.86}_{-0.48}$	$1.20^{+0.53}_{-0.36}$
HWL16a-056	0.470	$1.72^{+1.70}_{-0.96}$	$1.92^{+1.47}_{-0.90}$	$1.28^{+0.72}_{-0.52}$	$1.71^{+1.71}_{-0.95}$	$1.75^{+1.48}_{-0.81}$	$1.20^{+0.72}_{-0.50}$
HWL16a-057	0.450	$1.50^{+1.70}_{-0.93}$	$1.71^{+1.93}_{-0.77}$	$1.23^{+0.84}_{-0.51}$	$1.28^{+1.57}_{-0.84}$	$1.63^{+2.08}_{-0.74}$	$1.19^{+0.84}_{-0.50}$
HWL16a-058	0.248	$2.42^{+2.84}_{-1.28}$	$1.43^{+0.80}_{-0.50}$	$1.11^{+0.47}_{-0.37}$	$2.23^{+2.69}_{-1.21}$	$1.37^{+0.81}_{-0.49}$	$1.06^{+0.48}_{-0.37}$
HWL16a-059	0.561	$1.76^{+3.61}_{-1.33}$	$0.96^{+0.87}_{-0.67}$	$0.72^{+0.61}_{-0.52}$	$2.24^{+4.66}_{-1.60}$	$1.05^{+0.85}_{-0.68}$	$0.80^{+0.61}_{-0.53}$
HWL16a-060	0.469	$0.96^{+0.91}_{-0.59}$	$4.29^{+2.06}_{-1.72}$	$2.25^{+0.95}_{-0.89}$	$0.97^{+0.96}_{-0.61}$	$4.09^{+2.10}_{-1.80}$	$2.14^{+0.98}_{-0.91}$
HWL16a-064	0.144	$0.32^{+0.69}_{-\rm N/A}$	$3.03^{+2.19}_{-2.23}$	$0.99^{+0.95}_{-0.41}$	$0.26^{+0.71}_{-\rm N/A}$	$1.10^{+3.58}_{-0.45}$	$0.88^{+0.77}_{-0.36}$
HWL16a-070	0.645	$0.82^{+0.83}_{-0.60}$	$4.10^{+2.57}_{-1.95}$	$2.07^{+1.10}_{-0.99}$	$0.87^{+0.85}_{-0.60}$	$3.94^{+2.51}_{-1.92}$	$2.01^{+1.10}_{-0.99}$
HWL16a-071	0.534	$1.10^{+1.65}_{-0.82}$	$1.43^{+1.24}_{-0.65}$	$1.05^{+0.59}_{-0.46}$	$1.08^{+1.58}_{-0.79}$	$1.47^{+1.34}_{-0.66}$	$1.07^{+0.62}_{-0.46}$
HWL16a-076	0.296	$4.09^{+4.52}_{-1.93}$	$1.61^{+0.69}_{-0.37}$	$1.29^{+0.44}_{-0.29}$	$4.10^{+4.95}_{-1.98}$	$1.58^{+0.63}_{-0.36}$	$1.27^{+0.40}_{-0.29}$

Table 5. (Continued)

ID	z_{cl}	WMAP9 cosmology c_{200c}	M_{200c} $[10^{14}h^{-1}M_\odot]$	M_{500c} $[10^{14}h^{-1}M_\odot]$	Planck2018 cosmology c_{200c}	M_{200c} $[10^{14}h^{-1}M_\odot]$	M_{500c} $[10^{14}h^{-1}M_\odot]$
HWL16a-077	0.294	$3.84^{+5.92}_{-2.02}$	$1.25^{+0.53}_{-0.40}$	$0.99^{+0.36}_{-0.31}$	$3.80^{+5.93}_{-2.01}$	$1.28^{+0.55}_{-0.40}$	$1.02^{+0.37}_{-0.32}$
HWL16a-080	0.312	$3.04^{+2.74}_{-1.39}$	$2.32^{+1.43}_{-0.69}$	$1.80^{+0.74}_{-0.49}$	$2.99^{+2.92}_{-1.41}$	$2.23^{+1.35}_{-0.63}$	$1.75^{+0.72}_{-0.46}$
HWL16a-081	0.283	N/A	$1.19^{+0.37}_{-0.32}$	$0.97^{+0.28}_{-0.26}$	N/A	$1.20^{+0.36}_{-0.33}$	$0.98^{+0.28}_{-0.27}$
HWL16a-084	0.549	$0.33^{+1.02}_{-\mathrm{N/A}}$	$1.15^{+2.41}_{-0.70}$	$0.78^{+0.75}_{-0.45}$	$0.31^{+1.04}_{-\mathrm{N/A}}$	$1.05^{+2.24}_{-0.64}$	$0.73^{+0.71}_{-0.43}$
HWL16a-088	0.528	$2.35^{+3.01}_{-1.44}$	$1.57^{+1.05}_{-0.61}$	$1.22^{+0.64}_{-0.47}$	$2.42^{+3.07}_{-1.43}$	$1.54^{+1.00}_{-0.60}$	$1.19^{+0.63}_{-0.46}$
HWL16a-090	0.295	$1.98^{+2.76}_{-1.18}$	$1.25^{+0.72}_{-0.43}$	$0.98^{+0.42}_{-0.33}$	$1.90^{+2.76}_{-1.17}$	$1.25^{+0.71}_{-0.44}$	$0.98^{+0.42}_{-0.33}$
HWL16a-091	0.523	$1.51^{+1.54}_{-0.86}$	$3.31^{+2.78}_{-1.43}$	$2.23^{+1.16}_{-0.72}$	$1.47^{+1.44}_{-0.82}$	$3.57^{+2.66}_{-1.70}$	$2.23^{+1.18}_{-0.75}$
HWL16a-093	0.286	$2.13^{+1.70}_{-0.95}$	$1.82^{+1.17}_{-0.80}$	$1.20^{+0.61}_{-0.42}$	$2.12^{+1.75}_{-0.97}$	$1.69^{+1.32}_{-0.71}$	$1.18^{+0.64}_{-0.41}$
HWL16a-094	0.592	$0.95^{+0.78}_{-0.57}$	$10.90^{+5.99}_{-4.25}$	$5.59^{+2.00}_{-1.76}$	$0.85^{+0.78}_{-0.56}$	$10.51^{+5.91}_{-4.19}$	$5.26^{+1.95}_{-1.71}$
HWL16a-095	0.304	$3.97^{+2.49}_{-1.42}$	$3.07^{+1.30}_{-1.03}$	$2.26^{+0.76}_{-0.65}$	$3.81^{+2.41}_{-1.38}$	$3.07^{+1.37}_{-1.08}$	$2.24^{+0.81}_{-0.67}$
HWL16a-097	0.220	$2.30^{+4.30}_{-1.40}$	$1.00^{+0.52}_{-0.38}$	$0.79^{+0.36}_{-0.30}$	$1.89^{+3.24}_{-1.17}$	$0.95^{+0.54}_{-0.39}$	$0.75^{+0.37}_{-0.30}$
HWL16a-098	0.395	$0.38^{+1.03}_{-\mathrm{N/A}}$	$1.27^{+1.89}_{-0.53}$	$0.94^{+0.56}_{-0.37}$	$0.55^{+1.31}_{-\mathrm{N/A}}$	$1.24^{+1.30}_{-0.49}$	$0.95^{+0.51}_{-0.36}$
HWL16a-0101	0.152	$7.60^{+8.72}_{-3.20}$	$2.22^{+0.67}_{-0.48}$	$1.77^{+0.47}_{-0.37}$	$6.87^{+7.78}_{-2.91}$	$2.19^{+0.72}_{-0.50}$	$1.75^{+0.49}_{-0.39}$
HWL16a-0102	0.287	$1.20^{+1.14}_{-0.71}$	$1.76^{+1.18}_{-1.04}$	$0.91^{+0.62}_{-0.44}$	$1.10^{+1.12}_{-0.68}$	$1.76^{+1.31}_{-1.11}$	$0.86^{+0.68}_{-0.41}$
HWL16a-0103	0.260	$5.71^{+11.68}_{-3.02}$	$1.15^{+0.45}_{-0.37}$	$0.92^{+0.33}_{-0.29}$	$5.21^{+9.56}_{-2.71}$	$1.22^{+0.48}_{-0.39}$	$0.97^{+0.34}_{-0.30}$
HWL16a-0104	0.350	$0.71^{+0.74}_{-0.51}$	$3.67^{+1.79}_{-1.41}$	$1.75^{+0.73}_{-0.65}$	$0.75^{+0.76}_{-0.52}$	$3.49^{+1.83}_{-1.43}$	$1.69^{+0.75}_{-0.67}$
HWL16a-0107	0.308	$1.99^{+1.75}_{-0.97}$	$1.55^{+1.28}_{-0.65}$	$1.09^{+0.61}_{-0.39}$	$1.90^{+1.70}_{-0.95}$	$1.50^{+1.39}_{-0.63}$	$1.08^{+0.63}_{-0.40}$
HWL16a-0110	0.323	$1.76^{+1.36}_{-0.84}$	$2.52^{+1.35}_{-1.20}$	$1.51^{+0.74}_{-0.63}$	$1.55^{+1.24}_{-0.77}$	$2.70^{+1.49}_{-1.33}$	$1.57^{+0.78}_{-0.69}$
HWL16a-0112	0.154	$6.34^{+7.26}_{-2.75}$	$2.12^{+0.71}_{-0.49}$	$1.69^{+0.48}_{-0.38}$	$6.10^{+6.96}_{-2.65}$	$2.17^{+0.75}_{-0.52}$	$1.72^{+0.51}_{-0.39}$
HWL16a-0114	0.402	$2.80^{+5.43}_{-1.90}$	$0.99^{+0.53}_{-0.40}$	$0.78^{+0.37}_{-0.31}$	$2.23^{+4.37}_{-1.60}$	$0.93^{+0.53}_{-0.41}$	$0.72^{+0.37}_{-0.31}$
HWL16a-0115	0.281	$6.52^{+12.45}_{-3.29}$	$1.68^{+0.55}_{-0.44}$	$1.35^{+0.39}_{-0.35}$	$6.99^{+15.38}_{-3.62}$	$1.71^{+0.56}_{-0.44}$	$1.38^{+0.39}_{-0.35}$
HWL16a-0117	0.338	$3.06^{+2.65}_{-1.36}$	$2.48^{+1.67}_{-0.76}$	$1.92^{+0.87}_{-0.54}$	$2.79^{+2.43}_{-1.27}$	$2.49^{+1.84}_{-0.80}$	$1.91^{+0.93}_{-0.55}$